Available online at www.sciencedirect.com
ScienceDirect
Comput. Methods Appl. Mech. Engrg. 411 (2023) 116045
Computer methods in applied mechanics and engineering
www.elsevier.com/locate/cma

Improved XFEM for multiple crack analysis: Accurate and efficient implementations for stress intensity factors

Long-Fei Wen[a,b], Rong Tian[a,b], Li-Xiang Wang[c,*], Chun Feng[c,d]

[a] CAEP Software Center for High Performance Numerical Simulation, Beijing, 100088, China
[b] Institute of Applied Physics and Computational Mathematics, Beijing, 100088, China
[c] Key Laboratory for Mechanics in Fluid Solid Coupling Systems, Institute of Mechanics, Chinese Academy of Sciences, Beijing, 100190, China
[d] School of Engineering Science, University of Chinese Academy of Sciences, Beijing, 100049, China

Received 17 January 2023; received in revised form 18 March 2023; accepted 2 April 2023
Available online 24 April 2023

Abstract

The extended finite element method (XFEM) has achieved unprecedented success in crack analysis. However, challenges still remain for a multiple crack simulation. One issue is the difficulty of level set construction, where cracks are generally represented by combinations of different level set functions. Another issue is the rapidly increasing condition number of the global stiffness matrix, which is even more severe than the single crack case. In order to overcome these issues, we make two improvements as follows. On the one hand, inspired by the discontinuous description via cover cutting in Numerical Manifold Method (and later phantom node method in XFEM), we propose a level set templated cover cutting method, which makes use of level set values to cut a nodal patch and then to add virtual nodes. This method, which combines the advantages of both the level set method and the cover cutting technique, is simple and straightforward to implement. The method also plays a role in templated subdivision of discontinuous elements and hence presents an efficient and robust integration scheme. On the other hand, we extend the Improved XFEM (IXFEM), previously proposed by our research group, to the scenario of multiple crack problems. The method fundamentally eliminates the daunting issues of linear dependence and ill-conditioning of the standard XFEM, because it uses an extra-dof-free singularity enrichment around the crack tip. Numerical studies on multiple crack problems show that the developed approach offers various advantages: (1) Highly accurate SIF evaluation over the standard XFEM; (2) Well-conditioning of the global stiffness matrix independent of the number of cracks — condition number being of the same order as the standard FEM; (3) Efficient and robust linear system solving and geometric computations. Thus the developed approach is well capable of modeling arbitrary multiple crack problems.

Keywords: Improved XFEM (IXFEM); Multiple cracks; Extra-dof-free singularity enrichment; Level set templated cover cutting; Stress intensity factor (SIF); Linear elastic fracture mechanics (LEFM)

1. Introduction

Modeling multiple cracks has always been a necessity in various fields, such as hydraulic fracturing simulation [1–3], dam safety evaluation [4,5], energetic material design [6], structural integrity assessment [7], etc. Linear

* Corresponding author.
E-mail address: wanglx@imech.ac.cn (L.-X. Wang).

https://doi.org/10.1016/j.cma.2023.116045
0045-7825/

elastic fracture mechanics (LEFM) provides a theoretical basis for such problems. In LEFM, stress intensity factor (SIF) plays a central role, since it is the single parameter that represents the singular field at the crack tip and drives crack propagation. Thus an accurate evaluation of SIFs is quite essential for subsequent failure analysis of various structures.

Due to the critical role that SIF plays in crack analysis, its computation has attracted broad attention. Tada et al. published three versions of SIF manuals in 1973 [8], 1985 [9] and 2000 [10], respectively. Murakami edited five volumes of SIF manuals, which were published respectively in 1987 (Volumes 1 and 2) [11], 1992 (Volume 3) [12] and 2001 (Volumes 4 and 5) [13]. These SIF manuals have been widely used in the engineering and scientific community.

At present, there are two kinds of approaches, i.e. the analytical and the numerical, to compute SIFs. Both approaches have its pros and cons. The analytical approach has the advantage of high efficiency, but is limited to specific geometric configurations and simple loading conditions. The numerical approach has the advantage of wide applicability, but its efficiency is generally constrained by the mesh scale. In order to apply to arbitrary geometric configurations and complex loading conditions, the numerical approach is often adopted. The popular numerical methods for crack analysis include but are not limited to: finite element method (FEM) [14], boundary element method (BEM) [15], numerical manifold method (NMM) [16], generalized/extended finite element method (G/XFEM) [17–20], meshless methods [21,22], scaled boundary finite element method (SBFEM) [23], continuous discontinuous element method (CDEM) [24], extended isogeometric analysis (XIGA) [25], virtual element method (VEM) [26], cracking elements method [27], etc.

Among these numerical methods, XFEM has received extensive attention in recent two-plus decades. First proposed by Belytschko and his coworkers in 1999 [28,29], XFEM has three outstanding advantages: (1) Independence of crack geometry on the simulation mesh; (2) No necessity of remeshing when a crack grows; and (3) High accuracy achieved on a relatively coarse mesh. Due to these outstanding advantages, XFEM has been implemented into the commercial software ABAQUS [30] and ANSYS [31], signaling the acceptance from the industrial community.

Though XFEM has achieved unprecedented success in crack analysis, it is still hindered by two major issues [32,33]: (1) The highly ill-conditioning of the global stiffness matrix; and (2) The inconsistency of energy transfer on the extra degrees of freedom (dofs) in dynamic analysis. A number of remarkable efforts have been made to overcome these two issues. On the first issue, we mention the Stable GFEM (SGFEM) by Babuška and Banerjee [34], the Orthonormalized GFEM (OGFEM) by Sillem et al. [35] and two variations of G/XFEM by Agathos et al. [36,37] among many others. The SGFEM [34] recovers well-conditioning by subtracting the original local approximation of G/XFEM to the FE interpolant. This method has been applied to fracture analysis in both 2D [38] and 3D [39]. In the OGFEM [35], the basis functions used are orthonormalized to remove all linear dependences. In Ref. [36], Agothos et al. used a novel form of enrichment together with the dof gathering technique to achieve improved conditioning. In Ref. [37], they introduced a procedure for the local near-orthogonalization of enrichment functions, which significantly improves the conditioning. On the second issue, we mention the works by Réthoré et al. [40], Prabel et al. [41] and Combescure et al. [42] in the context of XFEM and the work by Zheng et al. [43] in the context of NMM. In Refs. [40–42], the extra dofs are increasingly appended to the nodes after each time stepping to ensure energy consistency in dynamic analyses. In Ref. [43], the temporal discretization is put prior to the spatial discretization, so all the dofs are valid only within the current time step. In this way, the inconsistency of energy transfer on extra dofs can be resolved elegantly. Though this formulation was implemented in the frame of NMM, it can also be extended to that of G/XFEM.

In our previous studies, we owed the very root leading to the above two issues to the extra dofs introduced in XFEM. Therefore, we proposed the Improved XFEM (IXFEM) [44–49] based on an extra-dof-free partition of unity approximation [50]. Eliminating the extra dofs, IXFEM overcomes the daunting issues of linear dependence and inconsistency of energy transfer on extra dofs in a neat and unified manner. At present, this method has been successfully applied to the static and dynamic analyses of single crack problems. As for multiple crack problems, no systematic investigation has been conducted yet — the overall accuracy for SIF computation and the conditioning of the global stiffness matrix remains undiscovered. This study aims at the extension of IXFEM to the scenario of multiple cracks.

The investigation on multiple crack analysis with XFEM is active. Daux et al. [51] first studied arbitrary branched and intersecting cracks with XFEM. Belytschko et al. [52] modeled arbitrary discontinuities within XFEM. Budyn et al. [53] introduced a crack length control scheme into XFEM for arbitrary multiple crack propagation. Zi et al. [54]

applied XFEM to modeling multiple fatigue cracks. Mousavi et al. [55] proposed to use harmonic enrichment functions to treat multiple, intersecting and branched cracks in a unified manner. Richardson et al. [56] proposed a novel geometric cutting algorithm in XFEM for modeling geometrically elaborate crack propagation. Xu et al. [57] extended the junction enrichment in XFEM to the simulation of dynamic crack branching. Sutula et al. [58–60] developed a minimum energy approach for multiple crack propagation within XFEM. Chen et al. [61] extended the phantom node method proposed by Song et al. [62] to the scenario of multiple cracks using mesh cut technique. Ding et al. [63,64] developed a variable-node XFEM with local mesh refinement for modeling multiple discontinuities. Jafari et al. [65] implemented XFEM in the commercial software COMSOL to solve arbitrary (single and multiple) crack problems.

It can be seen that the conventional XFEM generally employs level set method to deal with multiple cracks, which are represented by different combinations of level set functions. This method is simple to implement and can easily describe the jump of derivatives. However, it is unsuitable for large deformation analysis, since it does not account for mesh topology update when large deformation occurs. For description of arbitrary deformations, the cover cutting method in the context of NMM [66–69] is a favorable choice. The method represents cracks by the so-called node splitting technique, which has a simple and intuitive meaning. In essence, this method falls into the category of re-meshing and thus is suitable for arbitrary deformations. The main difficulty of this method is the reconstruction of mesh topology, i.e. how to add virtual nodes and how to reconstruct the connectivity.

In order to overcome the reconstruction difficulty in cover cutting, in this study we propose a hybrid method — the level set templated cover cutting method. The idea of this method is to make use of level set values to cut a cover and then to add virtual nodes. The method, which combines the advantages of both the level set method and the cover cutting technique, is simple and straightforward to implement. The method also plays a role in templated subdivision of discontinuous elements and hence presents an efficient and robust integration scheme. The proposed method has been successfully integrated into the IXFEM framework for modeling multiple cracks. Numerical studies conducted for multiple crack problems show that the developed approach is accurate, efficient, robust and stable, and thus is well suitable for modeling multiple cracks.

The paper is organized as follows. Section 2 briefly gives the governing equations for LEFM. Section 3 elaborates the proposed hybrid method for geometric description of multiple cracks. Section 4 formulates the novel Improved XFEM (IXFEM) in particular for multiple cracks. Section 5 numerically discretizes the governing equations with IXFEM and details the templated integration scheme. Section 6 gives the interaction integral theory for extraction of stress intensity factors. Section 7 demonstrates several numerical examples on multiple crack analysis. In the last section, conclusions are drawn regarding the proposed approach.

2. Governing equations

As depicted in Fig. 1, a two-dimensional (2-D) linear elastic fracture mechanics (LEFM) problem containing multiple cracks is defined, and the governing equations for this problem read

$$\nabla \cdot \boldsymbol{\sigma} + \boldsymbol{b} = \boldsymbol{0} \quad \text{in } \Omega \tag{1}$$

where $\nabla\cdot$ is the divergence operator; $\boldsymbol{\sigma}$ is the stress tensor; and $\boldsymbol{b}$ is the body force vector.

The displacement boundary condition is

$$\boldsymbol{u} = \bar{\boldsymbol{u}} \quad \text{on } \Gamma_{\mathrm{u}} \tag{2}$$

where $\boldsymbol{u}$ is the displacement vector; and $\bar{\boldsymbol{u}}$ is the prescribed displacement vector on the displacement boundary Γ_{u}.

The traction boundary conditions are

$$\left.\begin{aligned} \boldsymbol{\sigma} \cdot \boldsymbol{n} &= \bar{\boldsymbol{t}} \quad \text{on } \Gamma_{\mathrm{t}} \\ \boldsymbol{\sigma} \cdot \boldsymbol{n} &= \boldsymbol{0} \quad \text{on } \Gamma_{\mathrm{c}} \end{aligned}\right\} \tag{3}$$

where $\bar{\boldsymbol{t}}$ is the applied traction force vector on the traction boundary Γ_{t} and $\boldsymbol{n}$ is the unit outer normal vector. A traction-free boundary condition is assumed on the crack surface Γ_{c}.

The linear elastic constitutive law is assumed

$$\boldsymbol{\sigma} = \mathbb{C} : \boldsymbol{\varepsilon} \tag{4}$$

where $\mathbb{C}$ is the elasticity tensor; and $\boldsymbol{\varepsilon}$ is the strain tensor.

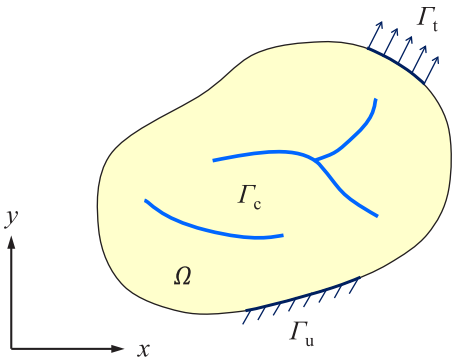

Fig. 1. Illustration for a 2-D LEFM problem containing multiple cracks.

Under small deformations, the strain–displacement relations read

$$\boldsymbol{\varepsilon} = \nabla_s \boldsymbol{u} = \frac{1}{2}\left(\nabla \boldsymbol{u} + (\nabla \boldsymbol{u})^T\right) \tag{5}$$

where ∇_s is the symmetric gradient operator.

3. Geometric description for multiple cracks

The geometric description approaches for multiple discontinuities (i.e. cracks herein and after) can be roughly divided into two categories: (1) the cover cutting method in the context of the numerical manifold method (NMM) and (2) the level set method in the context of the extended finite element method (XFEM).

The former represents cracks by the node splitting technique — the number of nodes after splitting is identical to the number of disconnected sub-regions cut by the discontinuities in the material domain (related to the crack distribution). This method has a simple and intuitive meaning. In essence, it belongs to the category of re-meshing and thus is suitable for arbitrary deformations. The main difficulty of this method is the reconstruction of mesh topology, including how to add virtual nodes and how to reconstruct the connectivity.

The latter represents cracks by the number of different combinations formed by level set values — the number of such combinations is equal to the number of disconnected sub-regions cut by cracks in the material domain. The number of extra degrees of freedom (dofs) is equal to the number of cracks, independent of the crack distribution. It should be less than the number of disconnected sub-regions. Essentially, this method represents discontinuities in function space and hence does not change the mesh topology. Therefore, the method is unsuitable for large deformation problems. In the case of small deformations, the two methods are equivalent to each other.

In this paper, we propose a third approach — level set templated cover cutting method, which combines the level set method and the cover cutting technique. It makes use of templated level set values in finite elements to cut a nodal patch and then to add virtual nodes. It avoids the difficulty of mesh topology reconstruction and inherits the advantage of the feasibility for arbitrary deformations. This novel approach will be detailed in Section 3.3.

3.1. Level set method

The conventional XFEM generally employs multiple sets of level set functions, which are naturally integrated into the step function enrichments, to solve multiple crack problems. The displacement field approximation has the following general form [51]

$$\boldsymbol{u}^h(\boldsymbol{x}) = \sum_{I\in\mathcal{I}} N_I(\boldsymbol{x})\boldsymbol{u}_I + \sum_{n=1}^{n_c}\sum_{J\in\mathcal{J}^n} N_J(\boldsymbol{x})\bar{H}_J^n(\boldsymbol{x})\boldsymbol{a}_J^n + \sum_{m=1}^{m_t}\sum_{K\in\mathcal{K}^m} N_K(\boldsymbol{x})\left(\sum_{\alpha=1}^{4}\bar{F}_{\alpha K}^m(\boldsymbol{x})\boldsymbol{b}_{\alpha K}^m\right) \tag{6}$$

where $\mathcal{I}$ is the set of all nodes, $\mathcal{J}^n$ the set of step enriched nodes related to the nth crack, $\mathcal{K}^m$ the set of singularity enriched nodes related to the mth crack tip; $N(\boldsymbol{x})$ is the standard FE shape function, $\bar{H}_J^n(\boldsymbol{x})$ the step enrichment function related to the nth crack, $\bar{F}_{\alpha K}^m(\boldsymbol{x})$ the singularity enrichment function related to the mth crack tip; n_c is the

number of cracks, m_t the number of crack tips; $\boldsymbol{u}_I$ is the translational dof vector at the Ith node, $\boldsymbol{a}_J^n$ the extra dof vector at the Jth node related to the nth crack, $\boldsymbol{b}_{\alpha K}^m$ the αth extra dof vector at the Kth node related to the mth crack tip.

The expression of $\bar{H}_J^n(\boldsymbol{x})$ is related to $\varphi_n(\boldsymbol{x})$, i.e. the normal level set function associated to the nth crack

$$\bar{H}_J^n(\boldsymbol{x}) = H\left(\varphi_n(\boldsymbol{x})\right) - H\left(\varphi_n(\boldsymbol{x}_J)\right) \tag{7}$$

where $H(x)$ is the Heaviside function

$$H(x) = \begin{cases} +1 & \text{for } x > 0 \\ -1 & \text{for } x < 0 \end{cases} \tag{8}$$

The expression of $\bar{F}_{\alpha K}^m(\boldsymbol{x})$ is given as

$$\bar{F}_{\alpha K}^m(\boldsymbol{x}) = F_\alpha^m(\boldsymbol{x}) - F_\alpha^m(\boldsymbol{x}_K) \tag{9}$$

where $F_\alpha(\boldsymbol{x})|_{\alpha=1}^4$ are the crack-tip singular functions

$$F_\alpha(\boldsymbol{x}) = \left\{ \sqrt{r}\cos\frac{\theta}{2}, \sqrt{r}\sin\frac{\theta}{2}, \sqrt{r}\sin\frac{\theta}{2}\sin\theta, \sqrt{r}\cos\frac{\theta}{2}\sin\theta \right\} \tag{10}$$

where (r, θ) is the crack-tip local (polar) coordinate system.

3.2. Cover cutting method

The basic idea of the cover cutting method in NMM is that when a nodal patch (a material domain surrounding a node) is completely cut into two by a discontinuity (such as a crack), the node is divided into two simultaneously. To be specific, as shown in Fig. 2a, a new node is added where the original node is located, and the two nodes describe the deformation and movement of the material separately on each side of the discontinuity.

For the sake of distinction, nodes falling outside the material domain are termed *virtual nodes*, e.g. i_1 in Fig. 2a. When a nodal patch is cut into more individual parts, more virtual nodes are added where the original node is located (Fig. 2b). If a nodal patch is cut into m parts, the original node will be split into one real node plus $(m-1)$ virtual nodes. As shown in Fig. 2b, i is the one real node and i_1, i_2 and i_3 are the three $(4-1=3)$ virtual nodes. The cover cutting method describes multiple cracks by increasing the number of nodes. The displacement field approximation for the cut elements can be expressed in the following form (the crack-tip singular enrichment is not considered temporarily)

$$\boldsymbol{u}^h(\boldsymbol{x}) = \sum_{I\in\mathcal{I}} N_I(\boldsymbol{x})\boldsymbol{u}_I + \sum_{J\in\mathcal{J}_{\text{add}}} N_J(\boldsymbol{x})\boldsymbol{u}_J \tag{11}$$

where $\mathcal{I}$ is the set of all nodes; $\mathcal{J}_{\text{add}}$ is the set of newly-added virtual nodes. The definitions of other symbols are consistent with Eq. (6). The same approximation form is adopted for both continuous and discontinuous problems, which is one of the advantages of the cover cutting method.

It is worth mentioning that the phantom node method proposed by Song et al. [62] for single crack problems in the context of XFEM is essentially the same as the cover cutting method in the context of NMM. In contrast for multiple crack problems, the cover cutting method has the advantage of more clear rules on how to add virtual nodes.

3.3. Proposed hybrid method

The proposed hybrid method, i.e. the level set templated cover cutting method, takes the following procedures (see Fig. 3). Firstly, each set of level set functions are constructed with regard to each crack (Fig. 3a). Note that different sets of level set functions are independent of each other. Secondly, the position of each crack in the finite elements is approximated based on each set of level set functions and the intersection points are calculated from zero level set values (Fig. 3b). Thirdly, by looking up a readily available cutting template (Fig. 3c), a parent cover is efficiently cut into two child ones (Fig. 3d). Meanwhile, virtual nodes are added to update the mesh topology (Fig. 3e). Lastly, if there is another crack crossing this parent cover, the previously formed child covers will be further cut by this subsequent crack (see Fig. 4), through repeating the previous three steps.

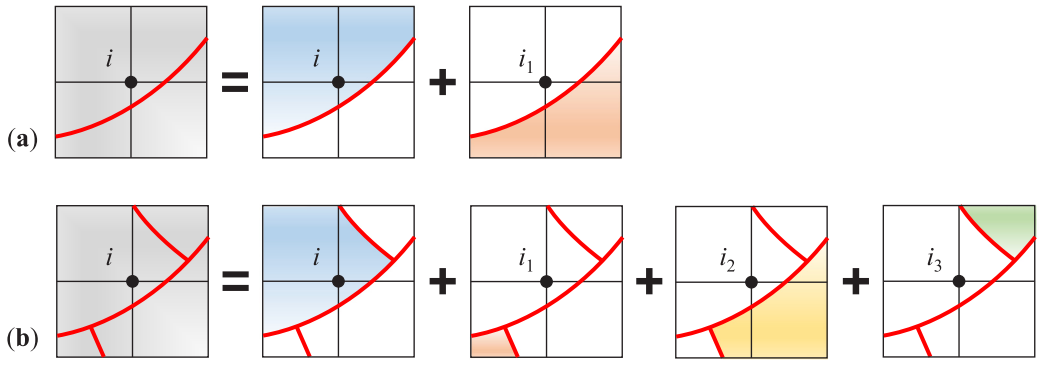

Fig. 2. Cover cutting method — discontinuities are represented by adding virtual nodes: (a) virtual node i_1 in a single crack case; (b) virtual nodes i_1, i_2 and i_3 in a multiple crack case.

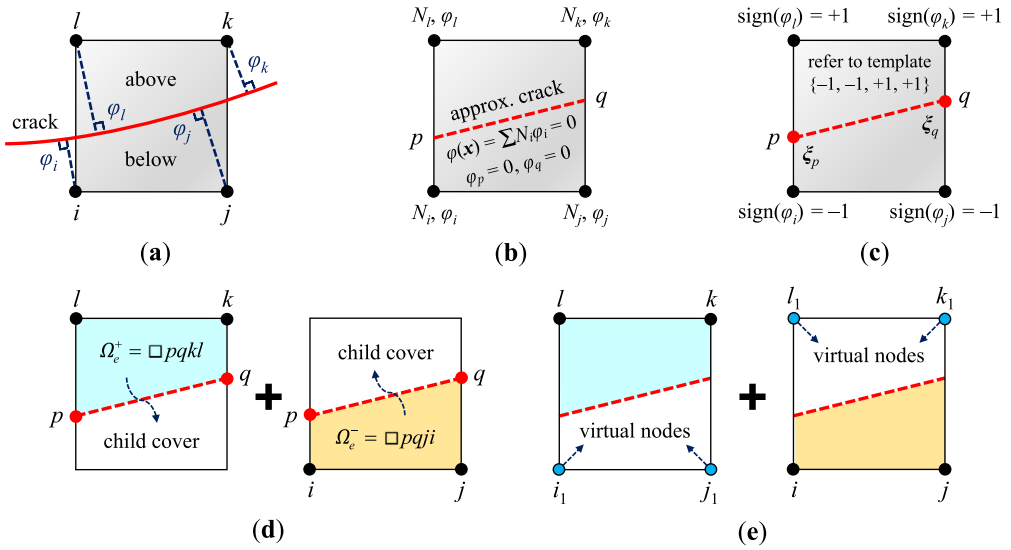

Fig. 3. Conceptualization for the proposed level set templated cover cutting method: (a) level set construction; (b) crack geometry approximation; (c) cutting template look-up; (d) cover cutting based on the template; (e) mesh topology update by adding virtual nodes.

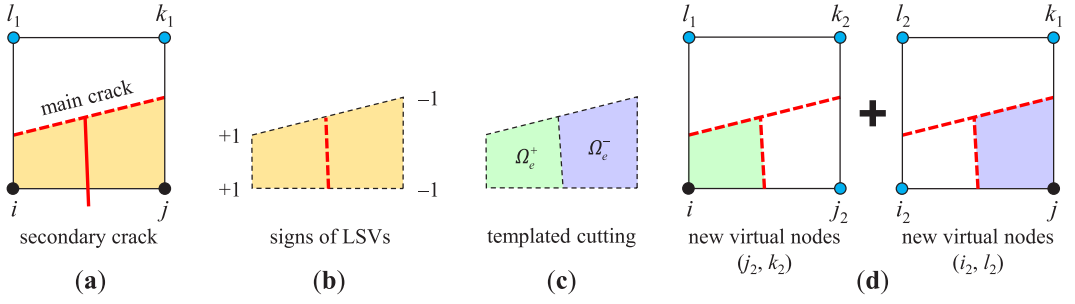

Fig. 4. Conceptualization for secondary cutting with the proposed method: (a) a secondary crack intersecting the main crack; (b) construction of level set values (LSVs) with regard to the secondary crack; (c) templated cutting of the child cover; (d) adding new virtual nodes.

3.3.1. Level set construction

We construct a set of level set functions for each crack. Each set of level set functions include a normal level set function and a tangential one. The normal level set function $\varphi(\boldsymbol{x})$ is defined as the minimum signed distance from a given point $\boldsymbol{x}$ to the crack surface Γ_{c}

$$\varphi_i(\boldsymbol{x}) = \min_{\bar{\boldsymbol{x}} \in \Gamma_{\mathrm{c},i}} \|\boldsymbol{x} - \bar{\boldsymbol{x}}\| \operatorname{sign}\left(\boldsymbol{n} \cdot (\boldsymbol{x} - \bar{\boldsymbol{x}})\right) \tag{12}$$

where the subscript i denotes the ith crack; $\|\cdot\|$ represents the Euclidean norm; $\boldsymbol{n}$ is the unit normal vector of Γ_{c}; and sign$(\cdot)$ stands for the sign function.

The tangential level set function $\psi(\boldsymbol{x})$ is defined as the signed distance from a given point $\boldsymbol{x}$ to the crack tip $\boldsymbol{x}_{\mathrm{t}}$

$$\psi_j(\boldsymbol{x}) = \boldsymbol{t} \cdot (\boldsymbol{x} - \boldsymbol{x}_{\mathrm{t},j}) \tag{13}$$

where the subscript j denotes the jth crack tip; and $\boldsymbol{t}$ is the unit vector tangent to the crack at the crack tip, pointing toward its exterior. Note that the number of crack tips may be greater than the number of cracks, since one crack may contain one or two crack tip(s).

The crack tip local (polar) coordinate system (r, θ) can be further defined in terms of the level set functions

$$r = r(\boldsymbol{x}) = \sqrt{\varphi^2(\boldsymbol{x}) + \psi^2(\boldsymbol{x})} \tag{14}$$

$$\theta = \theta(\boldsymbol{x}) = \arctan\left(\frac{\varphi(\boldsymbol{x})}{\psi(\boldsymbol{x})}\right) \tag{15}$$

3.3.2. Crack geometry approximation

The level set functions are approximated with standard finite element (FE) shape functions. The finite elements used in this study are 4-node quadrilaterals. The normal level set function $\varphi(\boldsymbol{x})$ in a finite element is given by

$$\varphi(\boldsymbol{x}) = \sum_{i=1}^{n_{\mathrm{en}}} \varphi_i N_i(\boldsymbol{\xi}), \quad \boldsymbol{x} \in \Omega_e \tag{16}$$

where φ_i are the nodal values of $\varphi(\boldsymbol{x})$; $N_i(\boldsymbol{\xi})$ are the standard FE shape functions in terms of the local coordinates $\boldsymbol{\xi}$; and n_{en} is the number of element nodes. The tangential level set function $\psi(\boldsymbol{x})$ does not need to be computed at this moment. The approximate crack position in a finite element Ω_e is given by

$$(\Gamma_{\mathrm{c}}^e)^h = \{\boldsymbol{x} \,|\varphi(\boldsymbol{x}) = 0, \quad \boldsymbol{x} \in \Omega_e\} \tag{17}$$

A linear interpolation gives the position of the intersection point p between the crack and the element edge ij:

$$\boldsymbol{\xi}_p - \boldsymbol{\xi}_i = \lambda(\boldsymbol{\xi}_j - \boldsymbol{\xi}_i) \tag{18}$$

where λ can be obtained from a linear interpolation of φ with $\varphi_p = 0$

$$\lambda = \frac{\varphi_p - \varphi_i}{\varphi_j - \varphi_i} = \frac{-\varphi_i}{\varphi_j - \varphi_i} \tag{19}$$

After manipulations, the coordinates of the intersection point p can be given by the coordinates and level set values at points i and j:

$$\boldsymbol{\xi}_p = \frac{\varphi_j \boldsymbol{\xi}_i - \varphi_i \boldsymbol{\xi}_j}{\varphi_j - \varphi_i} \tag{20}$$

3.3.3. Templated cover cutting

At first, we just consider the single crack case while performing cover cutting. For multiple cracks, deal with one crack at a time. Thus, the multiple crack case are decomposed into several single crack cases.

Based on our procedure, we first give the cutting templates for quadrilateral elements. The templates can be formed by the marching quadrilateral algorithm originally used in computer graphics. Here we show all the cutting templates in Fig. 5. The templates include four different patterns, i.e. a quadrilateral being cut into: (a) one triangle and one pentagon, (b) one triangle and one quadrilateral, (c) two triangles, or (d) two quadrilaterals. Accounting for

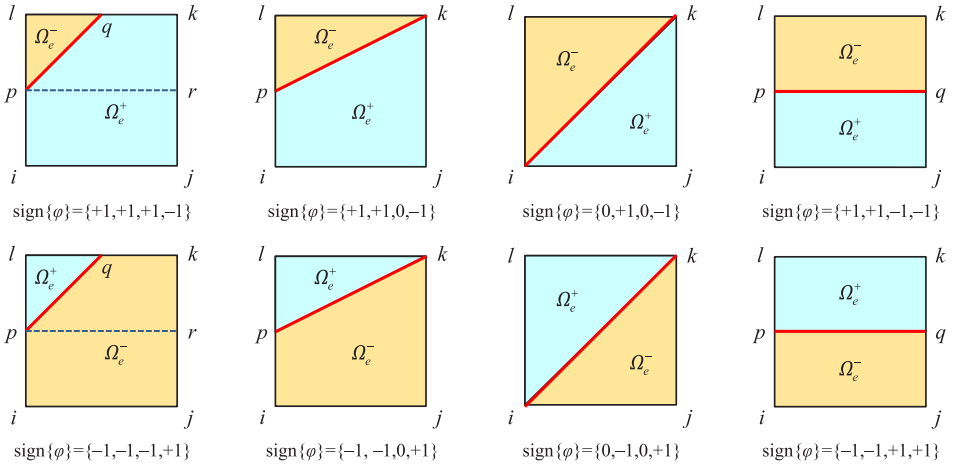

Fig. 5. The cutting templates for quadrilateral elements.

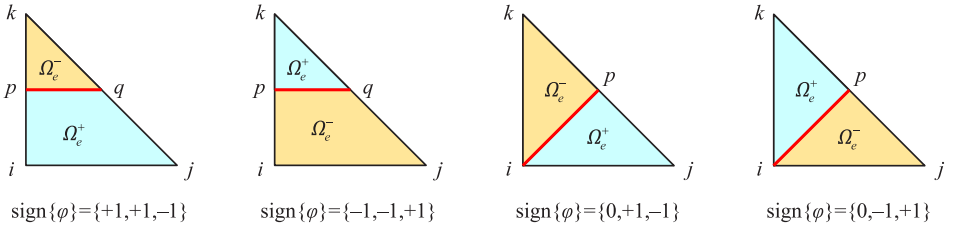

Fig. 6. The cutting templates for triangle elements.

the reverse situations, the cutting templates should be doubled. For the sake of simplicity and generality, we split the pentagon in pattern (a) into two quadrilaterals. Now all the resultant polygons are either triangles or quadrilaterals.

After a quadrilateral is cut by a primary crack, the resultant polygons may be cut by a secondary crack. In this case, the polygons are again cut by the template cutting algorithm. If the polygon is a quadrilateral, continue using the cutting templates in Fig. 5. If the polygon is a triangle, new cutting templates, formed by the marching triangle algorithm, should be used, as shown in Fig. 6. The same procedure goes for a third crack. After a cover is templatedly cut by all the cracks, virtual nodes are added where a node lies outside the material domain.

In order to understand how the templated cover cutting algorithm works for multiple cracks, we give a tree crack example, as shown in Fig. 7. The tree crack can be decomposed into three crack branches, i.e. Γ_1, Γ_2 and Γ_3. The cover around node P consists of four elements, i.e. A, B, C and D.

The cover is firstly cut by crack branch Γ_1. The level set functions are constructed with regard to Γ_1. From the signs of level set values, it is easy to know that the elements B, C and D are discontinuous elements, which can be cut according to the algorithm presented in Fig. 4. The element B is cut into subdomains B_1 (two quadrilateral cells) and B_2 (one triangle cell); the element C is cut into subdomains C_1 (one triangle cell) and C_2 (two quadrilateral cells); the element D is cut into subdomains D_1 (one quadrilateral cell) and D_2 (one quadrilateral cell).

The cover is then cut by crack branch Γ_2. The level set functions are constructed with regard to Γ_2. At this time, only the quadrilateral cell in subdomain D_2 is discontinuous and is cut into two subsubdomains (D_{21} and D_{22}). The cover is lastly cut by crack branch Γ_3. The level set functions are constructed with regard to Γ_3. The discontinuous subdomain comes to B_1, which contains two quadrilateral cells. One cell is cut into one triangle and one quadrilateral subcell; the other cell is cut into one triangle and two quadrilateral subcells.

After the cover is cut by all the cracks, four child covers are formed — {A, B_{11}, C_1, D_1}, {B_{12}}, {B_2, C_2, D_{22}} and {D_{21}}, and 13 subcells are generated. It is easy to know that P $\in$ {A, B_{11}, C_1, D_1}, so the split node in this child cover is a real node and the split nodes in other child covers are virtual nodes. The cover cutting is finished with mesh topology being updated.

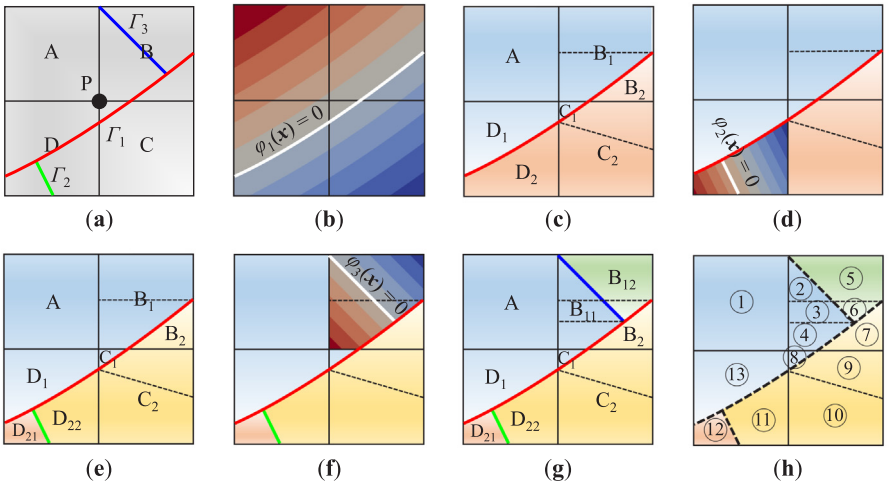

Fig. 7. Cover cutting example — the tree crack. (a) The cover composed of four elements (A, B, C and D) is to be cut by three crack branches (Γ_1, Γ_2 and Γ_3). (b) The level set function $\varphi_1(\boldsymbol{x})$ is constructed with regard to Γ_1. (c) The cover is firstly cut by crack branch Γ_1 based on cutting templates. (d) The level set function $\varphi_2(\boldsymbol{x})$ is constructed with regard to Γ_2. (e) The cover is secondly cut by crack branch Γ_2 based on cutting templates. (f) The level set function $\varphi_3(\boldsymbol{x})$ is constructed with regard to Γ_3. (g) The cover is lastly cut by crack branch Γ_3 based on cutting templates. (h) The cover is finally cut into four child covers and is subdivided into 13 subcells — child cover I (1, 2, 3, 4, 8, 13), child cover II (12), child cover III (7, 9, 10, 11), and child cover IV (5, 6).

Remark 1 (*Treatment for a Kinked Crack in a Cut Element*)**.** If a kinked crack exists in an element, special treatment is needed to maintain accuracy especially when the kink angle is large. Inspired by the virtual split element (VSE) technique proposed by Kumar et al. [70], we divide a cut element with a kink into two virtual cut sub-elements at the kink point. After the division, the level set templated cover cutting method can be applied to each sub-element with regard to each crack segment. Finally, the cover cutting gives the added virtual nodes and updated mesh topology. If a branched crack exists in an element, just use twice the above treatment at the branch point to get the final configuration.

Remark 2 (*Treatment for a Crack Close to a Node of a Cut Element*)**.** If a crack is close to a node of a cut element, the small portion (with area A_{min}) of the element (with area A_{tot}) will result in ill-conditioning of the global stiffness matrix. In order to tackle this issue, we adopt the area criterion presented by Dolbow et al. [71]. If the area ratio $A_{\text{min}}/A_{\text{tot}}$ is below a prescribed tolerance (e.g. 10^{-4}), the crack is moved toward the node of the element. We also mention the excellent work by Sanchez-Rivadeneira and Duarte [72], where they gave a good review on present remedies and proposed a node-snapping technique to overcome this issue.

Remark 3 (*On the Advantages of the Templated Cover Cutting Method*)**.** From the above procedures it is easy to learn that the proposed templated cover cutting method is very efficient and robust, since no cumbersome geometric implementations are introduced. It is also worth mentioning that the generated subcells will play a role in numerical integration of discontinuous elements, which will be discussed in Section 5.3.

4. Improved XFEM (IXFEM)

In this section, the Improved XFEM (IXFEM) is extended for multiple crack problems by integrating Eq. (11) with an extra-dof-free singularity enrichment [44–49]. A first glimpse of IXFEM for a single crack problem takes the following form

$$\boldsymbol{u}^h(\boldsymbol{x}) = \sum_{I\in\mathcal{I}/\mathcal{K}} N_I(\boldsymbol{x})\boldsymbol{u}_I + \sum_{J\in\mathcal{J}_{\text{add}}} N_J(\boldsymbol{x})\boldsymbol{u}_J + \sum_{K\in\mathcal{K}}\left(\sum_{L\in\mathcal{L}_K} N_L(\boldsymbol{x})\phi_K^L(\boldsymbol{x})\right)\boldsymbol{u}_K \tag{21}$$

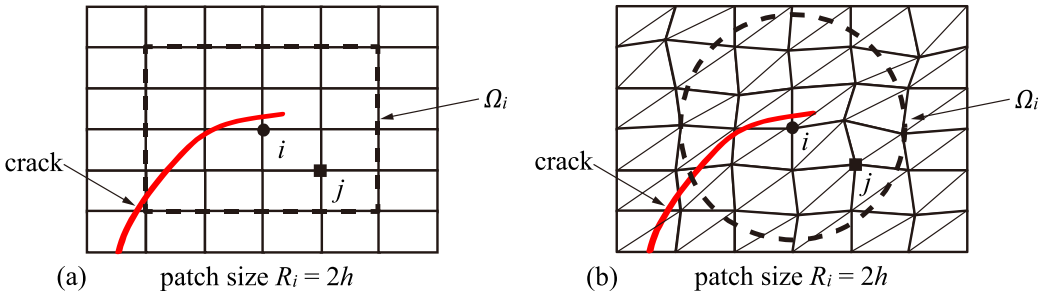

Fig. 8. Definition of a nodal influence domain for crack tip singularity enrichment: (a) structured mesh; (b) unstructured mesh.

where $\mathcal{K}$ is the set of crack-tip singularity enriched nodes, $\mathcal{L}_K \subset \mathcal{K}$ the subset related to node K; $\phi_K^L(\boldsymbol{x})$ is the local function around the crack tip. The last term in Eq. (21) is the so-called extra-dof-free singularity enrichment, which will be detailed next.

4.1. Extra-dof-free singularity enrichment

Denote Ω_{tip} as a subdomain containing the crack tip, in which all nodes are enriched with singular functions. Denote Ω_i as the nodal influence domain of node i, which is formed within radius R_i around node i, as illustrated in Fig. 8. In the nodal influence domain Ω_i, a local approximation of the displacement component $u_i(\boldsymbol{x})$ is constructed

$$u_i^{\text{loc}}(\boldsymbol{x}) = \boldsymbol{p}^{\mathrm{T}}(\boldsymbol{x})\boldsymbol{a}, \quad \boldsymbol{x} \in \Omega_i \tag{22}$$

$$u_i^{\text{loc}}(\boldsymbol{x}_i) = u_i \tag{23}$$

where $\boldsymbol{p}(\boldsymbol{x})$ is the basis vector and $\boldsymbol{a}$ is the unknown coefficient vector. Eq. (23) is the forced interpolation condition. Around the crack tip, we choose $\boldsymbol{p}(\boldsymbol{x})$ as

$$\boldsymbol{p}(\boldsymbol{x}) = \left[1, \frac{\boldsymbol{x}^{\mathrm{T}} - \boldsymbol{x}_k^{\mathrm{T}}}{R_i}, F_\alpha(\boldsymbol{x}) - F_\alpha(\boldsymbol{x}_k)\right]^{\mathrm{T}} \tag{24}$$

where the size of the nodal influence domain R_i is generally taken as $2 \sim 3$ times of the mesh size; and $F_\alpha(\boldsymbol{x})$ is defined in Eq. (10).

The L_2 norm is defined for the construction of the extra-dof-free enrichment

$$L = \frac{1}{2}\sum_{k\in\mathcal{P}_i}\left(\boldsymbol{p}^{\mathrm{T}}(\boldsymbol{x}_k)\boldsymbol{a} - u_k\right)^2 + \lambda\left(\boldsymbol{p}^{\mathrm{T}}(\boldsymbol{x}_i)\boldsymbol{a} - u_i\right) \tag{25}$$

where $\mathcal{P}_i$ is the node set in Ω_i; and λ is the Lagrange multiplier, to enforce the interpolation condition (23). Minimizing Eq. (25) by setting

$$\frac{\partial L}{\partial \boldsymbol{a}} = \boldsymbol{0}, \quad \frac{\partial L}{\partial \lambda} = 0 \tag{26}$$

one can obtain

$$\begin{bmatrix} \boldsymbol{A} & \boldsymbol{p}_i \\ \boldsymbol{p}_i^{\mathrm{T}} & \boldsymbol{0} \end{bmatrix}\begin{pmatrix} \boldsymbol{a} \\ \lambda \end{pmatrix} = \begin{pmatrix} \boldsymbol{P}\boldsymbol{u} \\ u_i \end{pmatrix} \tag{27}$$

where $\boldsymbol{p}_i = \boldsymbol{p}(\boldsymbol{x}_i)$; $\boldsymbol{A}$ is the moment matrix, $\boldsymbol{P}$ the basis-vector matrix, $\boldsymbol{u}$ the dof vector

$$\begin{cases} \boldsymbol{A} = \sum_{k\in\mathcal{P}_i} \boldsymbol{p}_k \boldsymbol{p}_k^{\mathrm{T}} \\ \boldsymbol{P} = \left[\boldsymbol{p}_1, \boldsymbol{p}_2, \ldots, \boldsymbol{p}_i, \ldots, \boldsymbol{p}_{n_i}\right] \\ \boldsymbol{u} = \left(u_1, u_2, \ldots, u_i, \ldots, u_{n_i}\right)^{\mathrm{T}} \end{cases} \tag{28}$$

where n_i is the node number in set $\mathcal{P}_i$.

Solving Eq. (27), we can obtain the unknown coefficient vector $\boldsymbol{a}$, and hence

$$u_i^{\text{loc}}(\boldsymbol{x}) = \sum_{k\in\mathcal{P}_i} \phi_k^i(\boldsymbol{x}) u_k \tag{29}$$

$$\phi_k^i(\boldsymbol{x}) = \boldsymbol{p}^{\mathrm{T}}(\boldsymbol{x}) \left(\boldsymbol{A}^{-1}\boldsymbol{p}_k - \frac{\boldsymbol{A}_{(1)}^{-1}\boldsymbol{A}_{(1)}^{-\mathrm{T}}\boldsymbol{p}_k}{\boldsymbol{A}_{11}^{-1}} + \frac{\boldsymbol{A}_{(1)}^{-1}\delta_{ik}}{\boldsymbol{A}_{11}^{-1}} \right) \tag{30}$$

where $\boldsymbol{A}_{(1)}^{-1}$ is the first column of $\boldsymbol{A}^{-1}$; $\mathbf{A}_{11}^{-1}$ is the first element of $\mathbf{A}_{(1)}^{-1}$; and δ is the Kronecker delta.

Taking Eq. (29) as the local approximation of the FE displacement field u_i in the nodal influence domain, we can get the new approximation as

$$u^h(\boldsymbol{x}) = \sum_i N_i(\boldsymbol{x}) u_i^{\text{loc}}(\boldsymbol{x}) = \sum_i \left[N_i(\boldsymbol{x}) \left(\sum_{k\in\mathcal{P}_i} \phi_k^i(\boldsymbol{x}) u_k \right) \right] \tag{31}$$

Rearranging the terms in Eq. (31), we finally get the extra-dof-free singularity enrichment around the crack tip

$$u^h(\boldsymbol{x}) = \sum_{i\in\mathcal{K}} \left(\sum_{k\in\mathcal{L}_i} N_k(\boldsymbol{x}) \phi_i^k(\boldsymbol{x}) \right) u_i = \sum_{i\in\mathcal{K}} N_i^{\text{tip}} u_i \tag{32}$$

where $\mathcal{L}_i$ is the set of nodal influence domains containing node i; $\phi_i^k(\boldsymbol{x})$ is the local function defined in the nodal influence domain Ω_k corresponding to node i. Replacing the indices i, k with K, L, respectively, gives the last term of Eq. (21).

4.2. IXFEM for multiple cracks

We extend Eq. (21) to the multiple crack scenario as

$$\boldsymbol{u}^h(\boldsymbol{x}) = \sum_{I\in\mathcal{I}/\mathcal{K}} N_I(\boldsymbol{x})\boldsymbol{u}_I + \sum_{n=1}^{n_{\text{c}}} \sum_{J\in\mathcal{J}_{\text{add}}^n} N_J(\boldsymbol{x})\boldsymbol{u}_J + \sum_{m=1}^{m_{\text{t}}} \sum_{K\in\mathcal{K}^m} \left(\sum_{L\in\mathcal{L}_K^m} N_L(\boldsymbol{x})\phi_K^L(\boldsymbol{x}) \right) \boldsymbol{u}_K \tag{33}$$

where $\mathcal{I}$ is the set of all nodes; $\mathcal{J}_{\text{add}}^n$ is the set of newly-added virtual nodes related to the nth crack outside the crack-tip enrichment domain; $\mathcal{K}^m$ is the set of singularity enriched nodes related to the mth crack tip; $\mathcal{L}_K^m \subset \mathcal{K}^m$ is the set of nodal influence domains containing node K related to the mth crack tip. The definitions of other symbols are consistent with Eq. (21).

4.3. Blending element treatment

Blending elements are the ones that contain both standard FE nodes and singularity enriched nodes (see Fig. 9). To ensure the accuracy and convergence of XFEMs, blending elements need special treatment [73]. A successful implementation for such treatment is the blending function (or ramp function) introduced by [74]

$$R(\boldsymbol{x}) = \begin{cases} 0 & \boldsymbol{x} \in \Omega_{\text{fem}} \\ \sum_{I=1}^{n_{\text{en}}} N_I(\boldsymbol{x}) & \boldsymbol{x} \in \Omega_{\text{blend}} \\ 1 & \boldsymbol{x} \in \Omega_{\text{tip}} \end{cases} \tag{34}$$

where Ω_{fem} denotes the standard FE domain, Ω_{blend} the blending element domain, Ω_{tip} the crack-tip singularity enriched domain; and n_{en} is the number of nodes in a blending element.

After introducing the blending function (34) into Eq. (33), we obtain the following IXFEM approximation

$$\boldsymbol{u}^h(\boldsymbol{x}) = \sum_{I\in\mathcal{I}/(\mathcal{K}+\mathcal{K}^*)} N_I(\boldsymbol{x})\boldsymbol{u}_I + \sum_{n=1}^{n_{\text{c}}} \sum_{J\in\mathcal{J}_{\text{add}}^n/\mathcal{K}^*} N_J(\boldsymbol{x})\boldsymbol{u}_J + \sum_{m=1}^{m_{\text{t}}} \sum_{K\in\mathcal{K}^m+\mathcal{K}_m^*} \tilde{N}_{mK}^{\text{tip}}(\boldsymbol{x})\boldsymbol{u}_K \tag{35}$$

$$\tilde{N}_{mK}^{\text{tip}}(\boldsymbol{x}) = (1 - R(\boldsymbol{x}))\, N_K(\boldsymbol{x}) + R(\boldsymbol{x}) \sum_{L\in\mathcal{L}_K^m} N_L(\boldsymbol{x})\phi_K^L(\boldsymbol{x}) \tag{36}$$

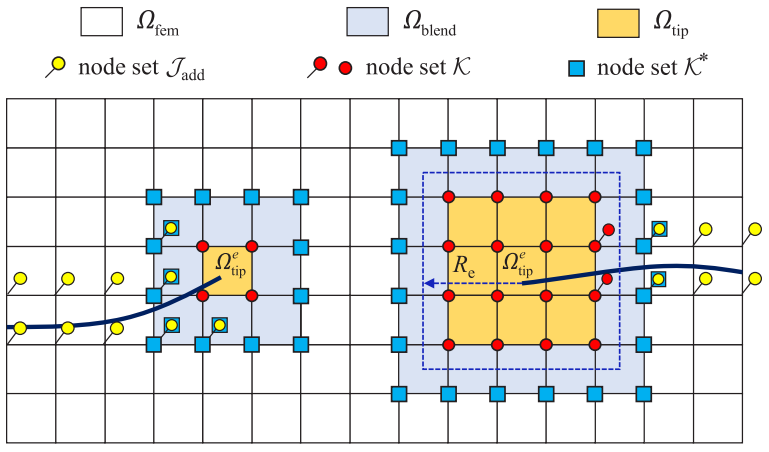

(a) Topological enrichment (Ω^e_{tip}) (b) Geometrical enrichment (R_e=2h)

Fig. 9. Notations for blending element treatment: (a) Topological enrichment: the singularity enrichment node set consists of all nodes belonging to elements containing the crack tip; (b) Geometrical enrichment: the singularity enrichment node set consists of all nodes for which $R < R_e$, where R_e is a user defined variable referred to as enrichment radius. In the figure, h denotes the crack-tip element size.

where $\mathcal{K}^* = \{i \,|\boldsymbol{x}_i \in \Omega_{\text{fem}} \cap \Omega_{\text{blend}}\}$ is the intersection node set between Ω_{fem} and Ω_{blend} (see Fig. 9); and $\mathcal{K}^*_m \subset \mathcal{K}^*$ is the intersection node set related to the mth crack tip. The definitions of other symbols are consistent with Eq. (33).

Remark 4 (*Criterion on Adding Virtual Nodes in a Crack-Tip Element*)**.** The criterion to add virtual nodes is whether the influence patch of a node, which consist of elements that contain the node, is completely cut by one (or more) crack(s). If the patch is completely cut by one (or more) crack(s), virtual nodes should be added and the topology should be updated accordingly. If the patch is partially cut by one crack (the case of nodes in a crack-tip element), no virtual nodes are added (Ω^e_{tip} in Fig. 9). In this case, the crack-tip element nodes do not need any special treatment.

Remark 5 (*Criterion on Selecting Crack-Tip Singularity Enriched Nodes*)**.** As for crack-tip singularity enrichment, both the real nodes and the virtual nodes are identical. If a virtual node falls into the crack-tip singularity enrichment domain, the virtual node should also be considered with the extra-dof-free singularity enrichment (Ω_{tip} in Fig. 9b). This treatment makes the presented approach straightforward and robust in implementation.

5. Numerical discretization

5.1. Weak form

According to the principle of virtual work, the equilibrium Eqs. (1) and the traction boundary conditions (3) can be transformed into the following weak integral form

$$\int_{\Omega} \delta\boldsymbol{\varepsilon} : \boldsymbol{\sigma}\, \mathrm{d}\Omega - \int_{\Omega} \delta\boldsymbol{u} \cdot \boldsymbol{b}\, \mathrm{d}\Omega - \int_{\Gamma_{\mathrm{t}}} \delta\boldsymbol{u} \cdot \bar{\boldsymbol{t}}\, \mathrm{d}\Gamma = 0 \tag{37}$$

where $\delta\boldsymbol{u}$ is the virtual displacement, and $\delta\boldsymbol{\varepsilon}$ the virtual strain.

Taking the linear elastic constitutive law (4) and the strain–displacement relations (5) into the weak form (37) gives

$$\int_{\Omega} (\nabla_{\mathrm{s}}\delta\boldsymbol{u}) : \mathbb{C} : (\nabla_{\mathrm{s}}\boldsymbol{u})\, \mathrm{d}\Omega - \int_{\Omega} \delta\boldsymbol{u} \cdot \boldsymbol{b}\, \mathrm{d}\Omega - \int_{\Gamma_{\mathrm{t}}} \delta\boldsymbol{u} \cdot \bar{\boldsymbol{t}}\, \mathrm{d}\Gamma = 0 \tag{38}$$

5.2. Discrete system of equations

After a Galerkin-type discretization (with Voigt notations) using the displacement field approximation (35), the weak form (38) of the governing equations can be discretized into the following system of linear equations:

$$\boldsymbol{K}\boldsymbol{U} = \boldsymbol{F} \tag{39}$$

where $\boldsymbol{K}$ is the global stiffness matrix; $\boldsymbol{U}$ is the global dof vector; and $\boldsymbol{F}$ is the global load vector. $\boldsymbol{K}$ and $\boldsymbol{F}$ can be expressed respectively as

$$\boldsymbol{K} = \int_{\Omega} \boldsymbol{B}^{\mathrm{T}} \boldsymbol{D} \boldsymbol{B} \, \mathrm{d}\Omega \tag{40}$$

$$\boldsymbol{F} = \int_{\Gamma_{\mathrm{t}}} \boldsymbol{N}^{\mathrm{T}} \bar{\boldsymbol{t}} \, \mathrm{d}\Gamma + \int_{\Omega} \boldsymbol{N}^{\mathrm{T}} \boldsymbol{b} \, \mathrm{d}\Omega \tag{41}$$

where $\boldsymbol{B}$ is the strain matrix; $\boldsymbol{D}$ is the elasticity matrix; and $\boldsymbol{N}$ is the shape function matrix. The global dof vector $\boldsymbol{U}$ together with the matrices $\boldsymbol{N}$ and $\boldsymbol{B}$ can be written respectively as

$$\boldsymbol{U} = \begin{bmatrix} \boldsymbol{U}_1^{\mathrm{T}} & \boldsymbol{U}_2^{\mathrm{T}} & \cdots & \boldsymbol{U}_p^{\mathrm{T}} \end{bmatrix}^{\mathrm{T}} \tag{42}$$

$$\boldsymbol{U}_I = \{u_I, v_I\}^{\mathrm{T}} \quad (I = 1, 2, \ldots, p) \tag{43}$$

$$\boldsymbol{N} = \begin{bmatrix} \boldsymbol{N}_1 & \boldsymbol{N}_2 & \cdots & \boldsymbol{N}_p \end{bmatrix} \tag{44}$$

$$\boldsymbol{N}_I = \begin{bmatrix} \tilde{N}_I & 0 \\ 0 & \tilde{N}_I \end{bmatrix} \quad (I = 1, 2, \ldots, p) \tag{45}$$

$$\boldsymbol{B} = \boldsymbol{L}\boldsymbol{N} = [\boldsymbol{L}\boldsymbol{N}_1 \quad \boldsymbol{L}\boldsymbol{N}_2 \quad \cdots \quad \boldsymbol{L}\boldsymbol{N}_p] \tag{46}$$

$$\boldsymbol{B}_I \equiv \boldsymbol{L}\boldsymbol{N}_I = \begin{bmatrix} \tilde{N}_{I,x} & 0 \\ 0 & \tilde{N}_{I,y} \\ \tilde{N}_{I,y} & \tilde{N}_{I,x} \end{bmatrix} \quad (I = 1, 2, \ldots, p) \tag{47}$$

where p is the total number of nodes; $\{u, v\}$ are the nodal dofs in x and y directions, respectively; $\boldsymbol{L}$ is the strain gradient operator; and $\tilde{N}_I$ are the generalized nodal shape functions.

Remark 6 (*On the Total Number of Nodes and Dofs*)**.** Note that the total number of nodes $p = p_{\mathrm{real}} + p_{\mathrm{virtual}}$ with p_{real} the number of real nodes and p_{virtual} the number of newly-added virtual nodes. Also note that all the nodal dofs $\{u_I, v_I\}$ are translational ones, so no extra dofs are introduced in the proposed approach and all the translational dofs come to a number of $2p$.

5.3. Numerical integration

In this study, numerical integration on discontinuous elements is implemented by subdivision of discontinuous elements. Actually, the templated cover cutting method, as shown in Section 3.3.3, also plays a role in subdivision of discontinuous elements. The resultant cut cells can be used for numerical integration.

Denote $\mathcal{N}_{\mathrm{cut}}^{\mathrm{cell}}$ as the number of cut cells in a *cut element* (i.e. an element fully cut by a crack) and $\mathcal{N}_{\mathrm{cut}}^{\mathrm{cgp}}$ as the number of Gauss points in each cut cell. A second-order Hammer integration scheme is applied for each cut cell and thus $\mathcal{N}_{\mathrm{cut}}^{\mathrm{cgp}} = 4$. The cut element stiffness associated to node i and node j can be written as [75]

$$\boldsymbol{K}_{ij}^{e} = \sum_{k=1}^{\mathcal{N}_{\mathrm{cut}}^{\mathrm{cell}}} \sum_{l=1}^{\mathcal{N}_{\mathrm{cut}}^{\mathrm{cgp}}} [\boldsymbol{B}_i(\boldsymbol{\xi}_{kl})]^{\mathrm{T}} \boldsymbol{D} [\boldsymbol{B}_j(\boldsymbol{\xi}_{kl})] \, |J(\xi_{kl})| \, W_{kl} \tag{48}$$

where $\boldsymbol{\xi}$ is the natural coordinates; $|J|$ is the determinant of Jacobian matrix; and W is the weight at Gauss point.

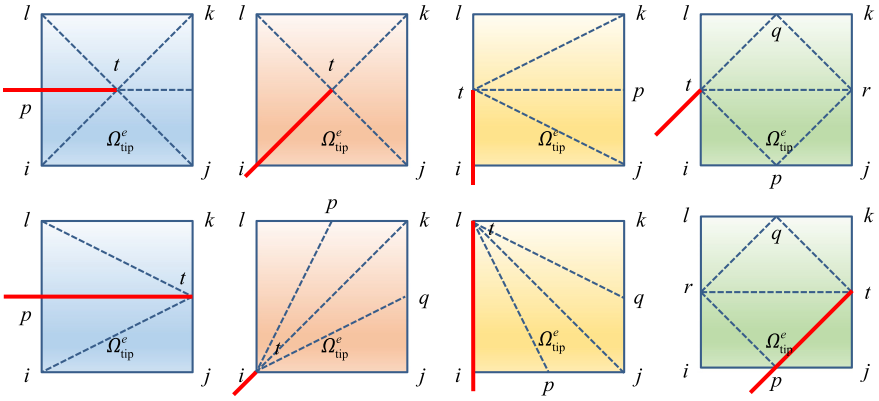

Fig. 10. Subdivision templates for tip elements.

Note that the templated cover cutting algorithm only gives subdivision for cut elements. As for a *tip element* (i.e. an element partially cut by a crack), new subdivision templates should be implemented, as shown in Fig. 10.

Denote $\mathcal{N}_{\text{tip}}^{\text{cell}}$ as the number of tip cells in a tip element and $\mathcal{N}_{\text{tip}}^{\text{cgp}}$ as the number of Gauss points in each tip cell. A sixth-order Hammer integration scheme is employed for each tip cell and thus $\mathcal{N}_{\text{tip}}^{\text{cgp}} = 13$. This scheme is selected with consideration of the tradeoff between accuracy of numerical integration and efficiency of stiffness matrix generation [44,45]. There are other quadrature rules to enhance accuracy and/or efficiency in the literature; we refer to Refs. [76–79] for details. The tip element stiffness associated to node i and node j can be written as [75]

$$\boldsymbol{K}_{ij}^{e} = \sum_{k=1}^{\mathcal{N}_{\text{tip}}^{\text{cell}}} \sum_{l=1}^{\mathcal{N}_{\text{tip}}^{\text{cgp}}} [\boldsymbol{B}_i(\boldsymbol{\xi}_{kl})]^{\mathrm{T}} \boldsymbol{D} [\boldsymbol{B}_j(\boldsymbol{\xi}_{kl})] \, |J(\xi_{kl})| \, W_{kl} \tag{49}$$

where the definitions of other symbols are consistent with Eq. (48).

6. Calculation of stress intensity factors

Stress intensity factor (SIF) is of critical importance in LEFM analysis because it is the single parameter that represents the singular field at the crack tip and drives crack propagation. The common methods to extract SIFs include: displacement extrapolation method [80], virtual crack extension method [81], virtual crack closure technique [82], interaction integral method [83], etc.

Among these methods, the interaction integral method is an effective energy approach which is based on the J-integral concept [84], and is widely used in the extraction of mixed-mode SIFs [85]. The domain form interaction integral is defined as

$$I^{(1,2)} = \int_A \left[W^{(1,2)} \delta_{1j} - \sigma_{ij}^{(1)} \frac{\partial u_i^{(2)}}{\partial x_1} - \sigma_{ij}^{(2)} \frac{\partial u_i^{(1)}}{\partial x_1} \right] \frac{\partial q}{\partial x_j} \, \mathrm{d}A \tag{50}$$

where σ_{ij}, ε_{ij}, u_i represent the stress tensor, the strain tensor and the displacement vector, respectively; the superscripts (1) and (2) denote the real field and the auxiliary field, respectively; A is the integral area enclosed by contours Γ, C_0, C_+, and C_- (see Fig. 11); q is a smoothing function, being 1 on the innermost contour and 0 on the outermost contour and varying linearly in between; and $W^{(1,2)}$ is the interaction strain energy

$$W^{(1,2)} = \frac{1}{2} \left(\sigma_{ij}^{(1)} \varepsilon_{ij}^{(2)} + \sigma_{ij}^{(2)} \varepsilon_{ij}^{(1)} \right) = \sigma_{ij}^{(1)} \varepsilon_{ij}^{(2)} = \sigma_{ij}^{(2)} \varepsilon_{ij}^{(1)} \tag{51}$$

The interaction integral is related to the SIFs of both real field and auxiliary field

$$I^{(1,2)} = \frac{2}{E_{\text{eff}}} \left(K_{\text{I}}^{(1)} K_{\text{I}}^{(2)} + K_{\text{II}}^{(1)} K_{\text{II}}^{(2)} \right) \tag{52}$$

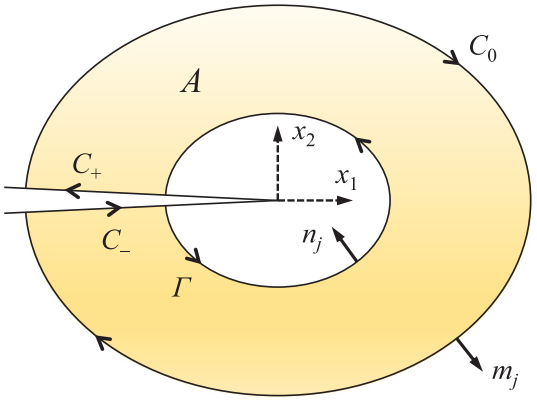

Fig. 11. Notations for the domain form interaction integral. The integral area A is enclosed by contours Γ, C_0, C_+, and C_-, and its outer unit normal vector is m_j.

where the effective Young's modulus E_{eff} is defined in terms of the material parameters E (Young's modulus) and ν (Poisson's ratio)

$$E_{\text{eff}} = \begin{cases} E, & \text{plane stress} \\ \frac{E}{1-\nu^2}, & \text{plane strain} \end{cases} \tag{53}$$

By setting, respectively, $K_{\text{I}}^{(2)} = 1$, $K_{\text{II}}^{(2)} = 0$ and $K_{\text{I}}^{(2)} = 0$, $K_{\text{II}}^{(2)} = 1$ in Eq. (52), one can obtain the mode I and mode II SIFs

$$K_{\text{I}}^{(1)} = \frac{E_{\text{eff}}}{2} I^{(1,\,\text{mode I})}, \quad K_{\text{II}}^{(1)} = \frac{E_{\text{eff}}}{2} I^{(1,\,\text{mode II})} \tag{54}$$

In practical implementations, a square interaction integral domain A is used. This domain is discretized into a uniform mesh with 4×4 quadrilateral subcells and each of them is integrated by 6×6 Gauss quadrature. The dimension of domain A is adaptively determined to avoid interference from other cracks or the exterior boundary and hence to ensure the accuracy of SIF calculation by interaction integral [47]:

(1) When the computed crack tip is free of other cracks and the boundary, the dimension of each subcell in domain A is taken as the size of the crack-tip element ($1h$);
(2) When the computed crack tip is close to other cracks or the boundary, the dimension of each subcell in domain A is taken as $d_{\text{c,min}}/3$, where $d_{\text{c,min}}$ is the minimum distance from current crack tip to other cracks or the boundary;
(3) When the computed crack tip is interfered by other crack tips, the dimension of each subcell in domain A is taken as $d_{\text{t,min}}/5$, where $d_{\text{t,min}}$ is the minimum distance from current crack tip to the interfering ones.

7. Numerical examples

In this section, we apply the IXFEM to various multiple crack problems. The following two XFEMs are referred to for comparison purposes:

- XFEM (Belytschko and his coworkers, 1999) [28,29]: the standard XFEM without blending treatments.
- CXFEM (Fries, 2008) [73]: the corrected XFEM with blending element correction.

Firstly, a systematic investigation on SIF accuracy is carried out regarding the proposed approach. This novel approach is thoroughly benchmarked with four classic multiple crack examples, namely:

- the example of double edge cracks in a finite plate;
- the example of symmetrical branched crack in an infinite plate;
- the example of cross crack in a squared plate; and
- the example of two cracks emanating from a hole in a finite plate.

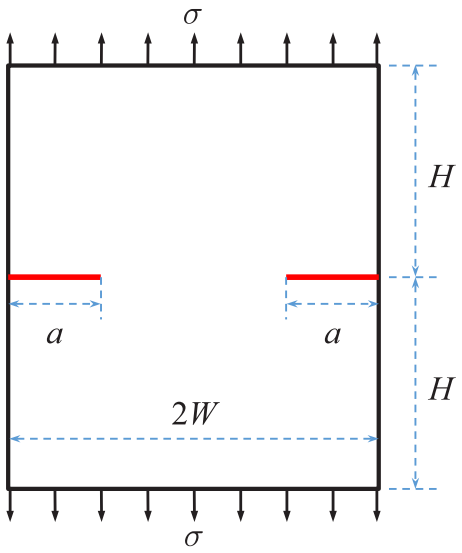

Fig. 12. Double edge cracks in a finite plate under uniaxial tension.

Secondly, the efficiency of the proposed approach is checked from the following three aspects:

- the first aspect is the efficiency of linear system solving. This is considered by the example of a square plate under uniaxial tension with many cracks (as many as 64). The conditioning of the global stiffness matrix and the expense of linear system solving is fully compared with those of the standard and corrected XFEMs.
- the second aspect is the efficiency of geometric calculations, i.e. crack cutting elements. This is checked by the example of a random test — generate a random quadrilateral element and a random crack and test the computation time of the proposed cutting method. The Delaunay triangulation method is taken as a reference.
- the third aspect is the efficiency of overall computations. This is studied by the double edge cracks example. We test the overall elapsed time of IXFEM to run this example and compare it with those of the standard and corrected XFEMs. It is worth mentioning that different crack-tip singularity enrichment domains are examined for all the three XFEMs in terms of overall computational efficiency.

Lastly, the proposed approach is applied to an engineering application — integrity assessment of an aircraft structural element with multiple site damage (MSD). The SIFs of cracks arising from MSD are analyzed and compared with existing software results.

7.1. SIF accuracy examples

7.1.1. Double edge cracks in a finite plate

We first examine the example of double edge cracks in a finite plate of width $2W$ and height $2H$ subjected to uniform uniaxial tensile stress σ, as shown in Fig. 12. The lengths of the double edge cracks are both a. A plane strain condition is assumed. A reference solution of mode I SIF to this problem exists [10]

$$K_{\mathrm{I}}^{\mathrm{ref}} = \sigma\sqrt{\pi a}\, g(\xi) \tag{55}$$

where $\xi = a/W$ and $g(\xi)$ is an empirical function

$$g(\xi) = (1.122 - 0.561\xi - 0.205\xi^2 + 0.471\xi^3 - 0.190\xi^4)/(1-\xi)^{1/2} \tag{56}$$

In the computations, the size of the plate is taken as $2W = 14$ and $2H = 21$, and the crack length is taken as $a = 3.5$. The material parameters are taken as: Young's modulus $E = 1000$ and Poisson's ratio $\nu = 0.3$. The uniaxial tensile stress is taken as $\sigma = 1$. The reference solution given by Eq. (55) is $K_{\mathrm{I}}^{\mathrm{ref}} = 3.9263$.

We consider all the numerical simulations with XFEM, CXFEM and IXFEM from the following two aspects:

Table 1
SIF results with different simulation meshes.

Mesh	Method	#DOFs	K_I	Error (%)
39 × 59	IXFEM	4880	3.9016	0.63
	XFEM	4936	3.8527	1.87
	CXFEM	5136	3.8959	0.77
59 × 89	IXFEM	10920	3.9136	0.32
	XFEM	10976	3.8833	1.10
	CXFEM	11176	3.9102	0.41
79 × 119	IXFEM	19360	3.9179	0.21
	XFEM	19416	3.9042	0.56
	CXFEM	19616	3.9181	0.21

Table 2
SIF results with different enrichment radii (R_e).

R_e	K_I			Error (%)		
	XFEM	CXFEM	IXFEM	XFEM	CXFEM	IXFEM
$1h$	3.8833	3.9102	3.9136	1.10	0.41	0.32
$2h$	3.9018	3.9196	3.9216	0.62	0.17	0.12
$3h$	3.9135	3.9232	3.9247	0.33	0.08	0.04
$4h$	3.9182	3.9256	3.9259	0.21	0.02	0.01
$5h$	3.9219	3.9262	3.9264	0.11	0.00	0.00
$6h$	3.9238	3.9265	3.9265	0.06	0.01	0.01
$7h$	3.9246	3.9267	3.9266	0.04	0.01	0.01
$8h$	3.9254	3.9268	3.9268	0.02	0.01	0.01
$9h$	3.9259	3.9269	3.9269	0.01	0.02	0.02
$10h$	3.9262	3.9270	3.9270	0.00	0.02	0.02

(1) One is the mesh convergence. We use different simulation meshes to study the SIF accuracy. The simulation meshes are taken as 39 × 59, 59 × 89, 79 × 119, respectively. In these simulations, only the topological enrichment strategy is used.
(2) The other is the enrichment convergence. Different enrichment domains are employed to also study the SIF accuracy. The simulation mesh is taken as 59 × 89. The enrichment radii (R_e) range from $1h$ to $10h$, with h the element size. Except for $R_e = 1h$, the remaining enrichment radii imply a geometrical enrichment strategy.

In the mesh convergence study, the SIF results, which are calculated on the three different meshes, are tabulated in Table 1. From this table, we can easily conclude that IXFEM generates more accurate SIF results than XFEM and CXFEM. The SIF errors by IXFEM are merely 0.63% on the 39 × 59 mesh, 0.32% on the 59 × 89 mesh, and 0.21% on the 79 × 119 mesh. In contrast, the SIF errors by XFEM are, respectively, 1.87%, 1.10% and 0.56%, which are almost one order of magnitude higher than those by IXFEM. The SIF errors by CXFEM are, respectively, 0.77%, 0.41% and 0.21%, which are slightly higher than those by IXFEM. However, for the three XFEMs, the accuracy of SIFs all converges with mesh refinement.

In the enrichment convergence study, the SIF results, which are calculated with 10 different enrichment domains, are tabulated in Table 2. From this table, we can draw several conclusions: (1) IXFEM generally produce more accurate SIF results than XFEM and CXFEM. The SIF accuracy of IXFEM is far better than that of XFEM and slightly better than that of CXFEM. (2) The geometrical enrichment produces better SIF results than the topological one by all the three XFEMs. Even using the smallest geometrical enrichment domain with $R_e = 2h$, the three XFEMs significantly decrease the SIF errors compared with the topological one. (3) For the three XFEMs, the accuracy of SIFs all converges with the radius of enrichment domain (R_e). We plot the curves of K_I against R_e in Fig. 13, which shows that the three numerical curves approach the analytical one with the increase of R_e.

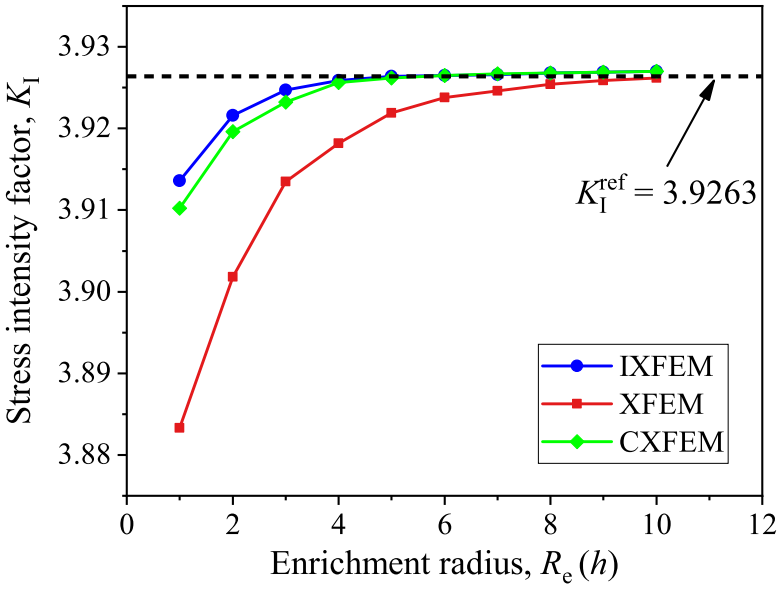

Fig. 13. Stress intensity factor versus enrichment radius.

7.1.2. Symmetrical branched crack in an infinite plate

We now test the example of symmetrical branched crack in an infinite plate subjected to uniform uniaxial tensile stress σ, as depicted in Fig. 14. The dimensions of the plate, which are $2W$ in width and $2H$ in height, are taken as large as possible to meet the far-field loading condition. The lengths of the main and secondary crack branches are a and b, respectively. The inclination angles of the two crack branches are both θ. A plane strain condition is assumed. The SIFs at the crack tips A and B are normalized by

$$F_{\mathrm{I}}^{\mathrm{A}} = \frac{K_{\mathrm{I}}^{\mathrm{A}}}{\sigma\sqrt{\pi c}}, \quad F_{\mathrm{I}}^{\mathrm{B}} = \frac{K_{\mathrm{I}}^{\mathrm{B}}}{\sigma\sqrt{\pi c}}, \quad F_{\mathrm{II}}^{\mathrm{B}} = \frac{K_{\mathrm{II}}^{\mathrm{B}}}{\sigma\sqrt{\pi c}} \tag{57}$$

where $2c = a + b\cos\theta$.

In the computations, the dimensions of the plate are taken as $2W = 40$ and $2H = 32$, the lengths of the crack branches are taken as $a = b = 1$, and the simulation mesh is taken as 333×265 with mesh size ratio $h/a = 0.12$. The material parameters are taken as: Young's modulus $E = 1000$ and Poisson's ratio $\nu = 0.3$. The uniaxial tensile stress is taken as $\sigma = 1$. The topological enrichment strategy is used in the tests, so the radius of crack-tip singularity enrichment domain is $R_e = 1h$.

We study the influence of different inclination angles θ on the SIF results. Five angles are considered, namely $\theta = 15°$, $30°$, $45°$, $60°$ and $75°$. We compare the SIF results from IXFEM with the standard XFEM by Daux et al. [51]. The SIFs given by Chen and Hasebe [86], which were calculated by the singular integral equation method (SIEM), are taken as a reference. It should be mentioned that the simulation mesh of IXFEM is intentionally taken as the same as that of XFEM in [51].

The SIFs calculated from IXFEM, XFEM and SIEM are tabulated in Table 3. The average difference between IXFEM and SIEM is calculated as 0.22% while the average difference between XFEM and SIEM is calculated as 0.88%. Therefore, we can conclude that the SIFs from IXFEM are in closer agreement with the reference solutions from SIEM than those from XFEM. We further plot the curves of normalized SIFs versus inclination angles, as shown in Fig. 15, which shows close agreement among the three methods. The von Mises stress contour for $\theta = 45°$ is presented in Fig. 16.

7.1.3. Cross crack in a square plate

We then inspect the example of cross crack in a square plate subjected to uniform biaxial tensile stress σ, as illustrated in Fig. 17. The size of the square plate $2W$ is taken as large as possible to meet the far-field loading

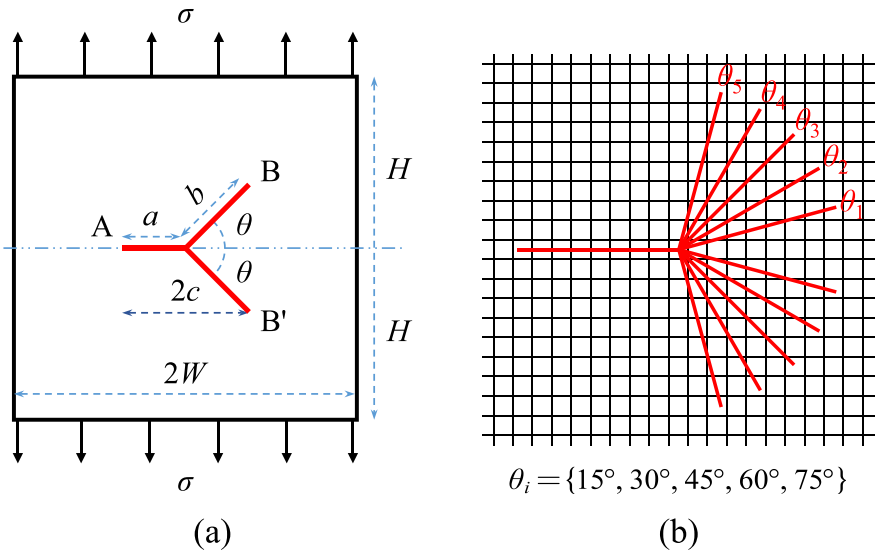

Fig. 14. Symmetrical branched crack in a plate under uniaxial tension: (a) model setup; (b) different crack configurations embedded in the simulation mesh.

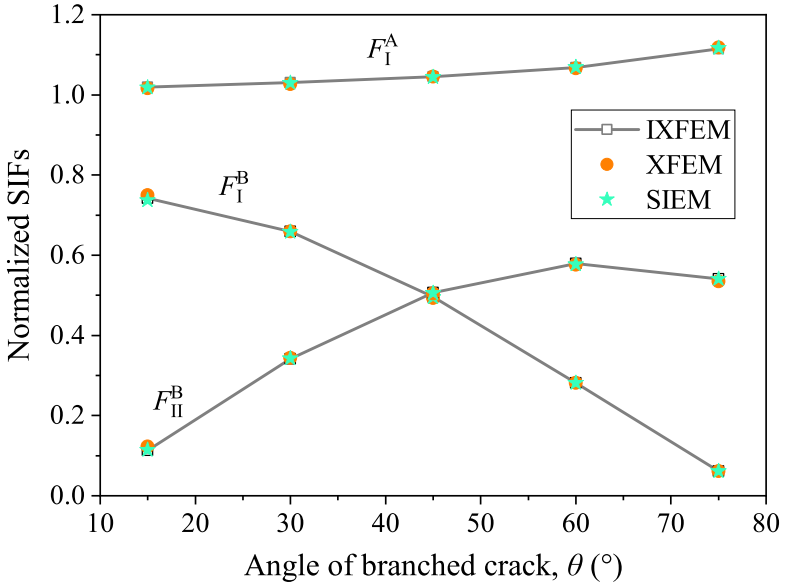

Fig. 15. Normalized SIFs versus inclination angle θ for the branched crack. Reference SIF solutions are taken from [51,86].

condition. The half lengths of the two perpendicular sets of the cross crack are both a. A plane strain condition is assumed. The SIFs at the four crack tips are normalized by

$$F_{\mathrm{I}} = \frac{K_{\mathrm{I}}}{\sigma\sqrt{\pi a}} \tag{58}$$

In the computations, the size of the plate is taken as $2W = 2$, the crack half-length a varies from 0.1 to 0.9, and the simulation mesh is taken as 99×99. The material parameters are taken as: Young's modulus $E = 1000$ and Poisson's ratio $\nu = 0.3$. The tensile stress is taken as $\sigma = 1$. The topological enrichment strategy is used in the tests, so the radius of crack-tip singularity enrichment domain is $R_{\mathrm{e}} = 1h$.

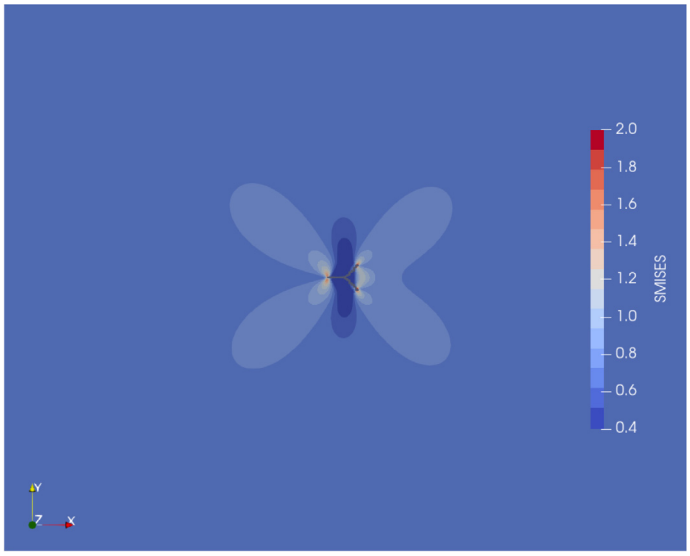

Fig. 16. von Mises stress contour of the branched crack when $\theta = 45°$.

Table 3
Normalized SIFs $F_{\mathrm{I}}^{\mathrm{A}}$, $F_{\mathrm{I}}^{\mathrm{B}}$, $F_{\mathrm{II}}^{\mathrm{A}}$ versus inclination angle θ.

SIF	Method	$\theta = 15°$	30°	45°	60°	75°
$F_{\mathrm{I}}^{\mathrm{A}}$	IXFEM	1.019	1.031	1.045	1.068	1.115
	XFEM[a]	1.016	1.027	1.045	1.066	1.118
	SIEM[b]	1.018	1.030	1.044	1.069	1.117
$F_{\mathrm{I}}^{\mathrm{B}}$	IXFEM	0.742	0.659	0.496	0.281	0.061
	XFEM[a]	0.750	0.659	0.493	0.281	0.061
	SIEM[b]	0.737	0.658	0.495	0.281	0.061
$F_{\mathrm{II}}^{\mathrm{A}}$	IXFEM	0.113	0.342	0.507	0.579	0.541
	XFEM[a]	0.123	0.344	0.504	0.576	0.535
	SIEM[b]	0.114	0.343	0.506	0.577	0.541

[a]The SIFs given by XFEM are taken from Daux et al. [51].
[b]The SIFs given by SIEM are taken from Chen and Hasebe [86].

Table 4
Normalized SIFs F_{I} for various dimension radios a/W.

Method	$a/W = 0.1$	0.2	0.3	0.4	0.5	0.6	0.7	0.8	0.9
IXFEM	0.8641	0.8840	0.9226	0.9557	1.0235	1.1308	1.3109	1.6237	2.3761
XFEM[a]	0.8653	0.8844	0.9147	0.9572	1.0253	1.1348	1.3170	1.6388	2.4395
FEM[b]	0.8641	0.8800	0.9092	0.9537	1.0223	1.1300	1.2866	1.4857	–

[a]The SIFs given by XFEM are taken from Daux et al. [51].
[b]The SIFs obtained by FEM are taken from Cheung et al. [87].

We study the influence of different crack dimensions a on the SIF results and compare the SIF results between IXFEM and two available numerical methods, namely the standard XFEM by Daux et al. [51] and the FEM by Cheung et al. [87]. It should be mentioned that the simulation mesh of IXFEM is intentionally taken as the same as that of XFEM in [51]. The normalized SIFs calculated from IXFEM, XFEM and FEM are tabulated in Table 4 for various dimension radios a/W.

From this table we can see that the SIFs obtained by the three methods gradually increase with the increase of a/W from 0.1 to 0.9. The SIF solutions by the three methods are very close to each other when $a/W \leq 0.6$. The SIF solutions by IXFEM are in better agreement with XFEM than FEM when $a/W > 0.6$. When the dimension

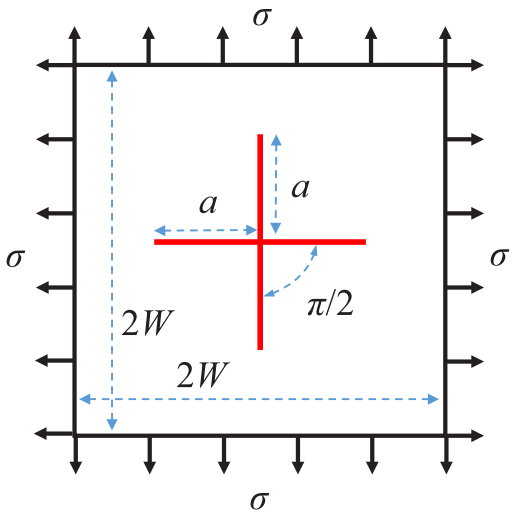

Fig. 17. Cross crack in a square plate under biaxial tension.

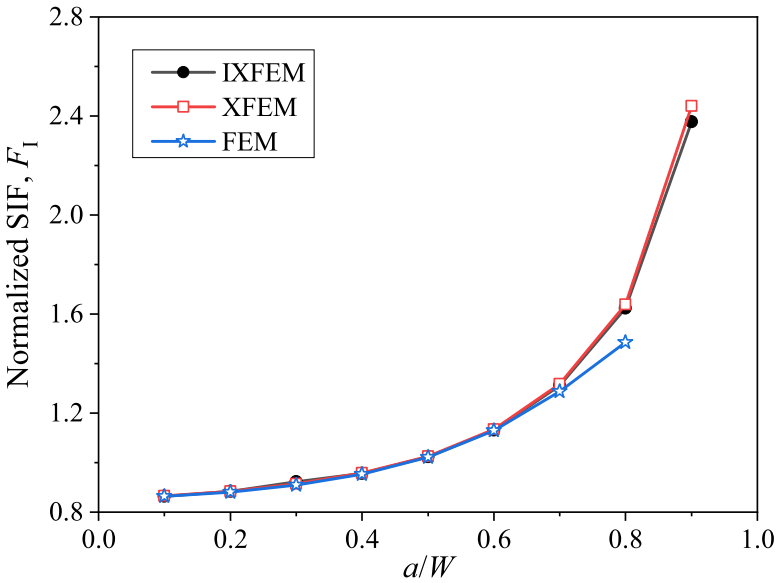

Fig. 18. Normalized SIF F_I versus dimension ratio a/W. Reference SIF solutions are taken from [51,87].

ratio a/W is very small, this problem degenerates into the problem of cross crack in an infinite plate subjected to biaxial tension, which has an analytical solution $F_{\mathrm{I}} = 0.8639$. When $a/W = 0.1$, the considered problem can be viewed as such a case. The SIF obtained by IXFEM is 0.8651, which is in better agreement with the analytical solution than XFEM. We further plot the curves of normalized SIF versus dimension ratio in Fig. 18, which shows good agreement among the three methods when $a/W \leq 0.6$. The von Mises stress contour for $a/W = 0.6$ is presented in Fig. 19. The stress distribution at the four crack tips is symmetrical about the intersection point, which is physically reasonable.

7.1.4. Two cracks emanating from a hole in a finite plate

We lastly check the example of two cracks emanating from a hole in a finite plate subjected to uniaxial tensile stress σ, as illustrated in Fig. 20a. The hole is centered in the plate and the two cracks are symmetrical about its center. The dimensions of the plate are $2W$ in width and $2H$ in height, the radius of the hole is r, and the distance

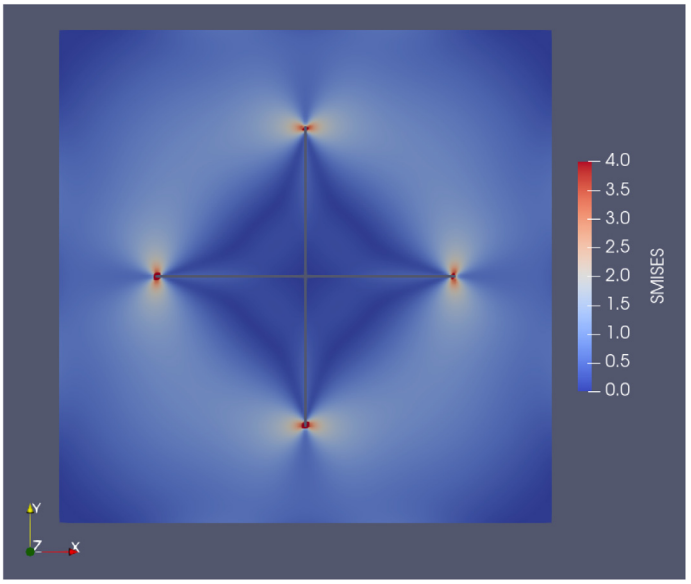

Fig. 19. von Mises stress contour of the cross crack when $a/W = 0.6$.

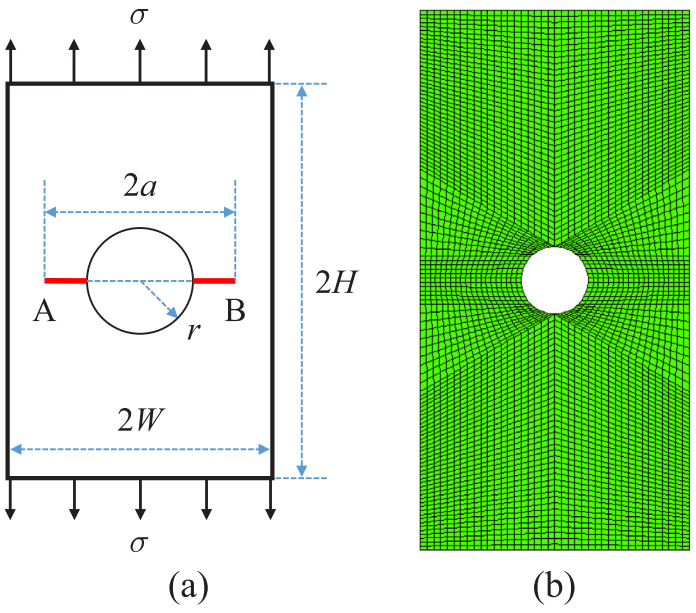

Fig. 20. Two cracks emanating from a hole in a finite plate under uniaxial tension: (a) model setup; (b) simulation mesh for IXFEM.

between the two tips is $2a$. A plane strain condition is assumed. The SIFs at the crack tips A and B are normalized by $F_{\mathrm{I}} = K_{\mathrm{I}}/(\sigma\sqrt{\pi a})$. In the computations, the dimensions of the plate are taken as $2W = 2$ and $2H = 4$. The radius of the hole is taken as $r = 0.25$. The tensile stress is taken as $\sigma = 1$. The simulation mesh contains 39×79 quadrilateral elements (Fig. 20b). The topological enrichment strategy is used in the tests, so the radius of crack-tip singularity enrichment domain is $R_{\mathrm{e}} = 1h$.

We study the influence of different crack tip distances $2a$ on the SIF results and compare the SIF results between IXFEM and the standard XFEM by Daux et al. [51]. The SIF solutions, obtained by the Improved Boundary

Table 5
Normalized SIFs F_{I} for various dimension radios a/W.

Method	$a/W = 0.4$	0.5	0.6	0.7	0.8	0.9
IXFEM	1.213	1.285	1.397	1.581	1.904	2.642
XFEM[a]	1.207	1.286	1.389	1.558	1.857	2.611
IBCM[b]	1.216	1.285	1.397	1.580	1.904	2.625

[a]The SIFs given by XFEM are taken from Daux et al. [51].
[b]The SIFs obtained by IBCM are taken from Newman Jr. [88].

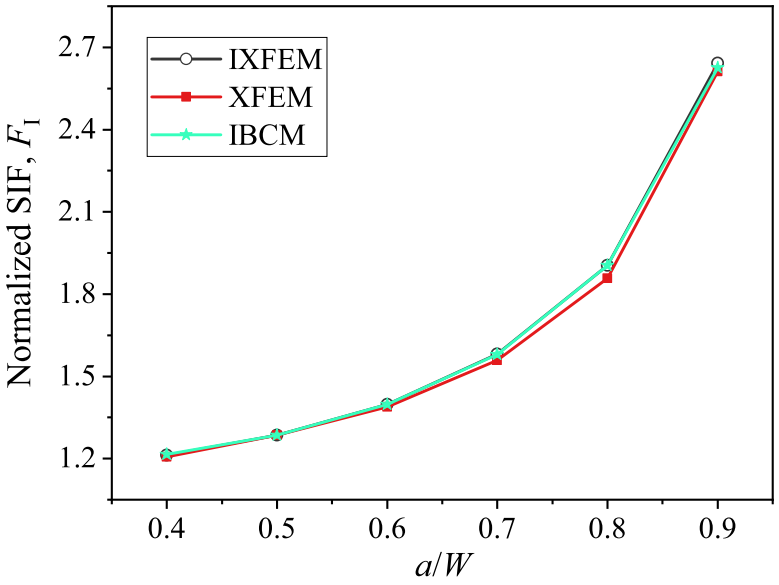

Fig. 21. Normalized SIF versus ratio a/W. Reference SIF solutions are taken from [51,88].

Collocation Method (IBCM) [88], are taken for a reference. The normalized SIFs calculated from the three methods are tabulated in Table 5 for various ratios a/W.

From the table we can observe that the SIFs given by the three methods gradually increase with the increase of a/W from 0.4 to 0.9 and that they are close to each other. By simple calculations, we know that the average difference between IXFEM and IBCM is merely 0.16% while the average difference between XFEM and IBCM could reach 0.96%. Therefore, we can conclude that the SIFs from IXFEM are in closer agreement with the reference solutions from IBCM than those from XFEM. We further plot the curves of normalized SIF versus ratio a/W, as shown in Fig. 21, which shows good agreement among the three methods. The von Mises stress contour for this problem when $a/W = 0.6$ is presented in Fig. 22.

7.2. Efficiency considerations

7.2.1. Efficiency in terms of linear system solving

We use the example of a square plate under uniaxial tension with 64 horizontal cracks, as illustrated in Fig. 23, to investigate efficiency of IXFEM in terms of linear system solving for multiple crack analysis. The size of the square plate is W and all the 64 cracks have a length of a. The distribution of the cracks is symmetrical and aligned, as shown in Fig. 23. The top side of the plate is subjected to a uniform tensile stress σ while the bottom side is fixed. The material parameters are Young's modulus E and Poisson's ratio ν.

In the tests, $W = 0.2$, $a = 0.012$, $\sigma = 1$, $E = 1000$ and $\nu = 0.3$. A 100×100 regular simulation mesh is considered and hence the mesh size is $h = 0.002$. The topological enrichment strategy is used in the tests, so the radius of crack-tip singularity enrichment domain is $R_{\mathrm{e}} = 1h$.

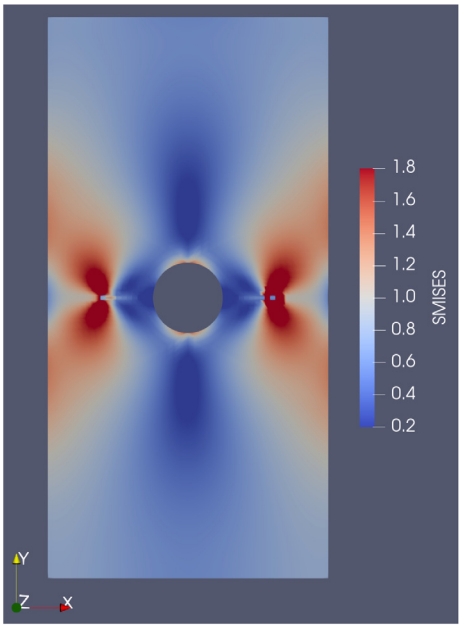

Fig. 22. von Mises stress contour for two cracks emanating from a hole when $a/W = 0.6$.

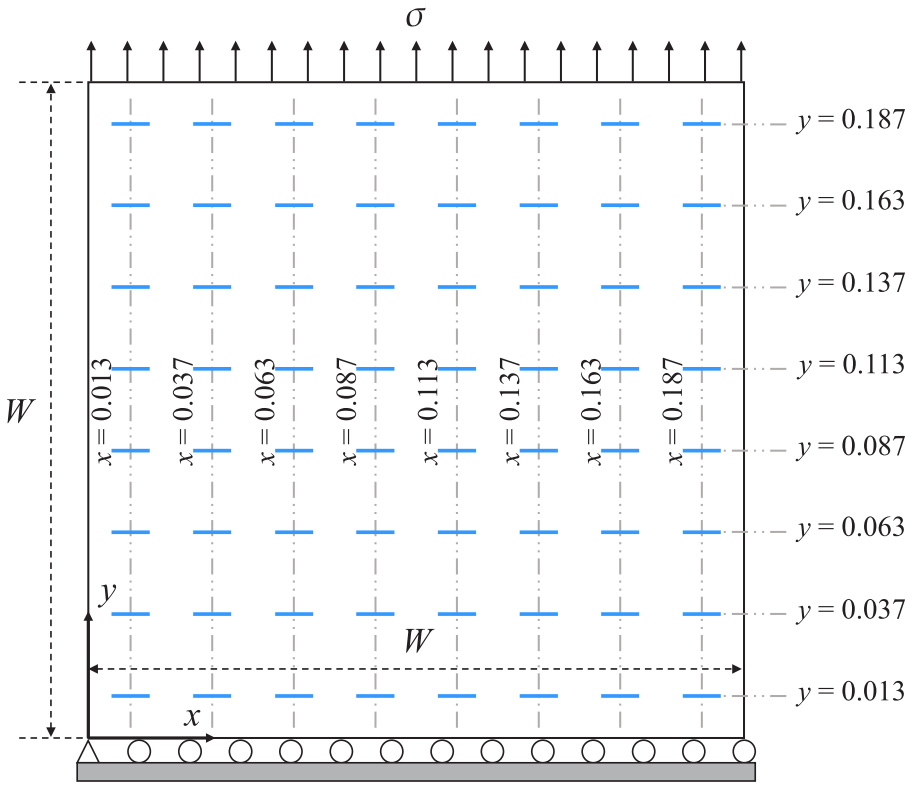

Fig. 23. A square plate under uniaxial tension with 64 horizontal and equal-length cracks. The distribution of cracks is symmetrical and aligned.

Table 6
Efficiency comparison among IXFEM, XFEM and CXFEM in terms of condition number and linear system solving expense.

n_c[a]	method	n_{dofs}[b]	λ_{max}[c]	λ_{min}[d]	C_N[e]	n_{iter}[f]	t_{LSS}[g]
0	FEM	20402	5.3826E+03	5.8230E−01	9.2437E+03	185	0.77
1	IXFEM	20418	6.0754E+03	5.8188E−01	1.0441E+04	187	0.77
	XFEM	20482	5.3826E+03	1.4000E−03	3.8447E+06	197	0.84
	CXFEM	20674	5.3826E+03	2.1946E−18	2.4527E+21	478	2.02
2	IXFEM	20434	6.0759E+03	5.8115E−01	1.0455E+04	194	0.79
	XFEM	20562	5.3826E+03	3.9811E−04	1.3520E+07	205	0.85
	CXFEM	20946	5.3826E+03	1.3484E−18	3.9918E+21	666	2.93
4	IXFEM	20466	6.0761E+03	5.7927E−01	1.0489E+04	198	0.81
	XFEM	20722	5.3825E+03	3.9628E−04	1.3583E+07	208	0.89
	CXFEM	21490	5.3825E+03	1.7491E−19	3.0773E+22	853	4.01
8	IXFEM	20530	6.0761E+03	5.7638E−01	1.0543E+04	201	0.85
	XFEM	21042	5.3825E+03	2.9258E−04	1.8397E+07	214	0.95
	CXFEM	22578	5.3825E+03	9.8334E−20	5.4737E+22	1171	6.35
16	IXFEM	20658	6.0806E+03	5.6887E−01	1.0690E+04	202	0.87
	XFEM	21682	5.3822E+03	2.9258E−04	1.8396E+07	222	1.03
	CXFEM	24754	5.3822E+03	5.8888E−20	9.1379E+22	1519	10.46
32	IXFEM	20914	6.0807E+03	5.5422E−01	1.0972E+04	209	0.95
	XFEM	23072	5.3811E+03	2.9258E−04	1.8392E+07	227	1.24
	CXFEM	29106	5.3811E+03	2.0433E−20	2.6341E+23	1743	17.49
64	IXFEM	21426	6.0807E+03	5.4979E−01	1.1060E+04	215	1.08
	XFEM	27522	5.3634E+03	2.7766E−04	1.9316E+07	235	1.54
	CXFEM	37810	5.3639E+03	1.6934E−20	3.1675E+23	2045	32.62

[a] n_c = number of cracks.
[b] n_{dofs} = number of degrees of freedom.
[c] λ_{max} = maximum eigenvalue of global stiffness matrix.
[d] λ_{min} = minimum nonzero eigenvalue of global stiffness matrix.
[e] C_N = condition number of global stiffness matrix.
[f] n_{iter} = number of iterations in linear system solving (BiCG).
[g] t_{LSS} = time cost for linear system solving (unit in second).

In consideration of that one of defacto solvers in large-scale simulations is the subspace iteration method, the biconjugate gradient (BiCG) method in the open-source library PETSc [89] is chosen to solve systems of linear equations (SLE). Considering the ill-conditioning of XFEM and CXFEM, the convergence tolerance is set to 10^{-8} on purpose and the maximum number of iterations is set to 50,000. The testing environment is a personal computer equipped with 32 GB random access memory (RAM) and an 8-core CPU, whose base frequency is 3.7 GHz.

During the tests, the cracks are gradually activated in a double-increase manner — firstly activate $2^0 = 1$ crack; secondly activate $2^1 = 2$ cracks; thirdly activate $2^2 = 4$ cracks; $\cdots$; and lastly activate $2^6 = 64$ (all) cracks. As a consequence, a total of 7 cases are considered, namely the cases with 1, 2, 4, 8, 16, 32 and 64 cracks.

The efficiency of linear system solving is considered for IXFEM, XFEM and CXFEM, respectively. Table 6 provides an efficiency comparison between the three XFEMs and the standard FEM. In the standard FEM, a crack-free problem is solved using the same mesh and boundary conditions as the three XFEMs adopt. The test results in Table 6 are detailed in terms of condition number of global stiffness matrix and linear system solving expense (reflected by iterations and time to solve SLE), which are discussed in details next.

The maximum eigenvalue λ_{max} and the minimum nonzero eigenvalue λ_{min} of the global stiffness matrices are computed for the three XFEMs and are compared with the standard FEM, as shown in Table 6. The condition number C_N, which is defined as $\lambda_{max}/\lambda_{min}$, is also given in this table. It is observed from the table that:

(1) The minimum nonzero eigenvalue of XFEM is $3 \sim 4$ orders of magnitude smaller than that of FEM; the minimum nonzero eigenvalue of CXFEM is $18 \sim 20$ orders of magnitude smaller than that of FEM. In contrast, the minimum nonzero eigenvalue of IXFEM is in the same order of magnitude as that of FEM.

Table 7
Comparison of condition number logarithms among IXFEM, XFEM and CXFEM.

$\log_2(n_c)$	$\log_{10}(C_N)$			
	FEM (no crack)	IXFEM	XFEM	CXFEM
0	3.965845317	4.018741447	6.58486407	21.3896367
1	3.965845317	4.019322375	7.13098902	21.6011734
2	3.965845317	4.020743876	7.13298188	22.4881694
3	3.965845317	4.022964207	7.26473940	22.7382803
4	3.965845317	4.028977705	7.26462643	22.9608443
5	3.965845317	4.040271383	7.26471520	23.4206277
6	3.965845317	4.043756741	7.28592687	23.5007211

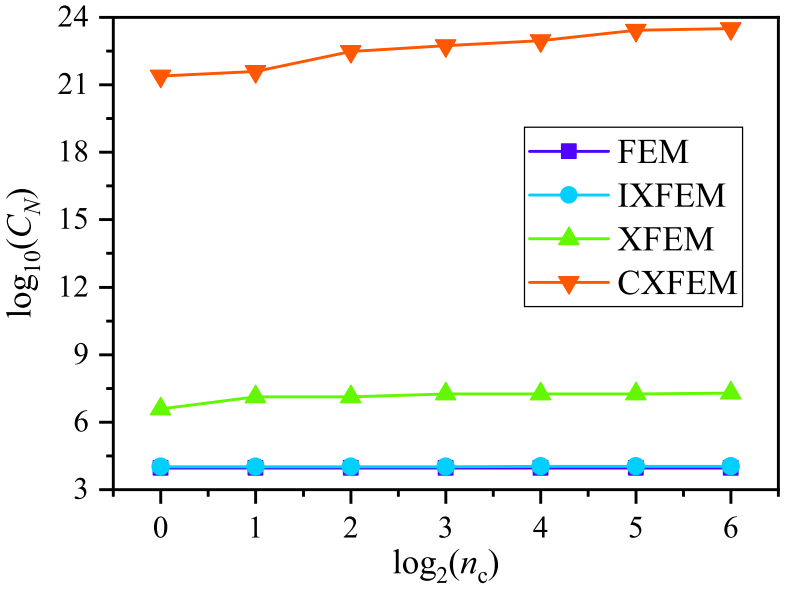

Fig. 24. Comparison of condition numbers among IXFEM, XFEM and CXFEM. The lines of XFEM and CXFEM are far above the line of IXFEM, while the lines of IXFEM and FEM coincide with each other.

(2) The condition number of XFEM is $2 \sim 3$ orders of magnitude larger than that of FEM; the condition number of CXFEM is $17 \sim 19$ orders of magnitude larger than that of FEM. In contrast, the condition number of IXFEM is in the same order of magnitude as that of FEM.
(3) As the number of cracks increases, the minimum nonzero eigenvalues of both XFEM and CXFEM somewhat decrease (XFEM decreases one order of magnitude whereas CXFEM decreases two orders of magnitude), while the minimum nonzero eigenvalue of IXFEM remains almost unchanged as FEM does.
(4) As the number of cracks increases, the condition numbers of XFEM and CXFEM somewhat increase as well (XFEM increases one order of magnitude whereas CXFEM increases two orders of magnitude), while the condition number of IXFEM remains almost unchanged as FEM does.

The logarithms of condition numbers are further computed for the three XFEMs in Table 7 and are plotted in Fig. 24. The table shows that the logarithms of condition numbers of XFEM and CXFEM (in particular) are much higher than that of IXFEM, which is nearly the same as that of FEM. We can also observe this point from the figure, where the lines of XFEM and CXFEM (in particular) are far above the line of IXFEM, while the lines of IXFEM and FEM coincide with each other.

From the above observations, we can conclude that: (1) the conditioning of IXFEM is as well as FEM, and is much better than XFEM and particularly CXFEM; (2) as the number of cracks increases, the ill-conditioning of XFEM and particularly CXFEM can become even more severe, whereas the well-conditioning of IXFEM remains almost unchanged as FEM does.

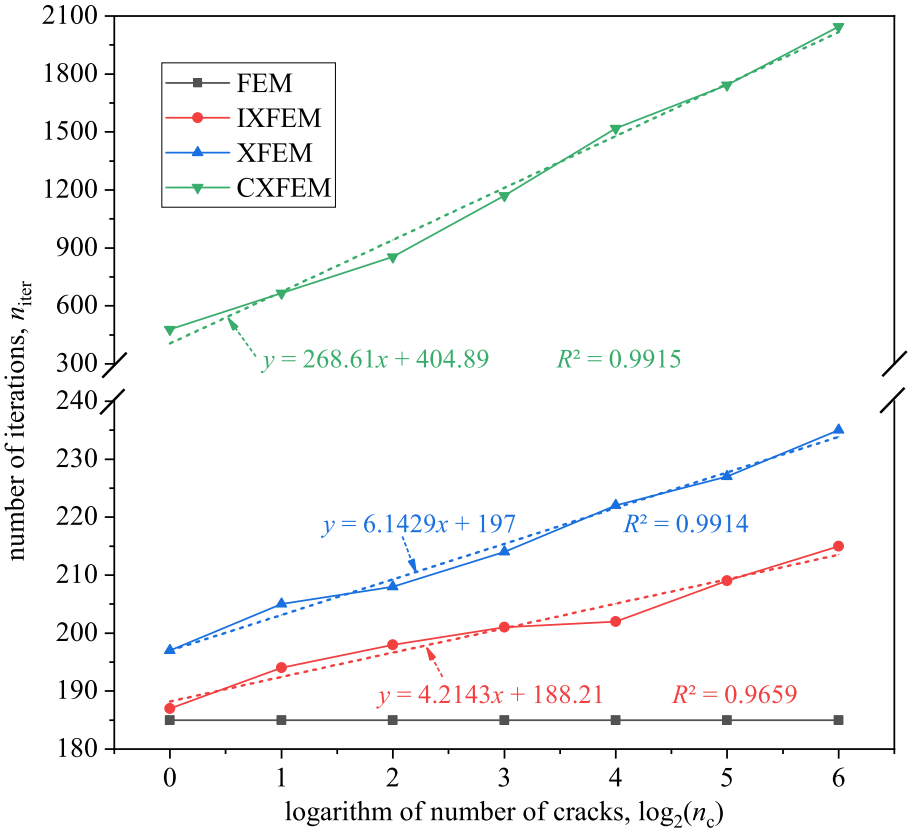

Fig. 25. Comparison of number of iterations (n_{iter}) versus logarithm of number of cracks ($\log_2(n_c)$) among IXFEM, XFEM and CXFEM. Dashed lines represent linear fitting curves.

The expense of the three XFEMs in terms of linear system solving is also investigated. The iterations and time to solve SLE are shown in Table 6. Detailed analysis on iterations to solve SLE is plotted in Fig. 25 while that on time is plotted in Fig. 26.

It can be observed from the table and figures that:

(1) IXFEM not only solves a relatively smaller size of system, but also converges faster than XFEM and CXFEM when dealing with multiple crack problems. In particular, IXFEM converges one magnitude of order faster than CXFEM.

(2) As the number of cracks increases, the number of iterations to solve SLE becomes larger for all the three XFEMs. A linear relation between the number of iterations and the logarithm of the number of cracks seems to exist (Fig. 25) and hence the number of iterations is of order $O(\log(n_c))$.

(3) The slopes of the linear relation are 4.2143 for IXFEM, 6.1429 for XFEM and 268.61 for CXFEM, respectively. The slope of IXFEM is the smallest among the three XFEMs, which means that the more the cracks, the relatively fewer iterations that IXFEM increases to solve SLE.

(4) As the number of cracks increases, the time to solve SLE becomes also longer for all the three XFEMs. A polynomial relation between the time to solve SLE and the logarithm of the number of cracks seems to exist (Fig. 26). A cubic polynomial fits the relation very well and hence the time to solve SLE is of order $O(\log^3(n_c))$.

(5) The major coefficients in the cubic relation are 0.0025 for IXFEM, 0.0047 for XFEM and 0.2664 for CXFEM, respectively. The coefficient of IXFEM is the smallest among the three XFEMs, which also means that the more the cracks, the relatively less time that IXFEM consumes to solve SLE.

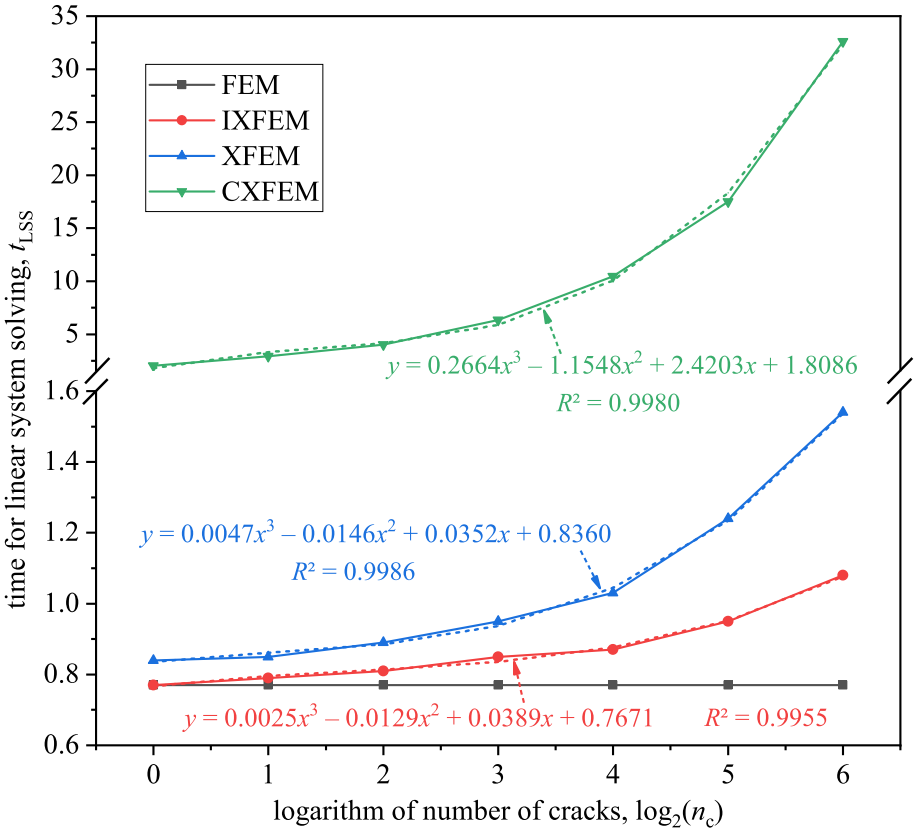

Fig. 26. Comparison of time for linear system solving (t_{LSS}) versus logarithm of number of cracks ($\log_2(n_c)$) among IXFEM, XFEM and CXFEM. Dashed lines represent cubic fitting curves.

From the above observations, we can find that IXFEM is highly efficient in terms of linear system solving, in particular for multiple crack problems. As the number of cracks increases, the ill-conditioning of XFEM and CXFEM can become even more severe, which leads to more expense of linear system solving. Since IXFEM remains well-conditioning in such problems, it consumes relatively less expense of linear system solving compared with the two XFEMs. Though some better solvers may exist to solve the ill-conditioned systems of the two XFEMs, it is still reasonably concluded that IXFEM is more robust and more stable and hence less challenging and less expensive in multiple crack analysis.

7.2.2. Efficiency in terms of geometric calculations

We use the example of a square plate, as illustrated in Fig. 27, to investigate the efficiency of the proposed templated cutting method in Section 3.3.3. The plate occupies domain $\Omega = [0, 2] \times [0, 2]$. The test procedures are as follows:

(1) Randomly generate four points A, B, C, D $\in \Omega$;
(2) Connect these points to make a convex quadrilateral element Ω_e = ABCD (assume this order) and this element is also randomly generated;
(3) Randomly generate two points, one (P) on the left side and the other (Q) on the right;
(4) Connect the two points P and Q to form a random crack Γ;
(5) Use the proposed templated cutting method to subdivide the element Ω_e;
(6) For comparison purposes, also use Delaunay triangulation to subdivide this element.
(7) Repeat the above procedures until a given looping number (e.g. 1000) is reached.

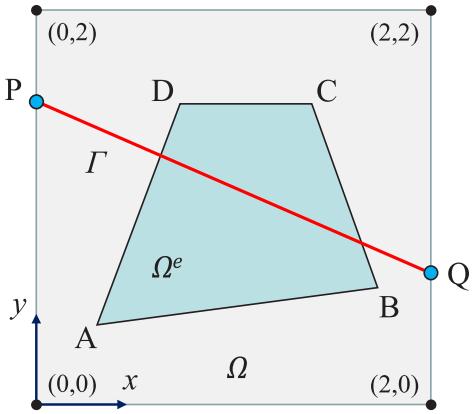

Fig. 27. Geometric setup for crack cutting test.

Table 8
Comparison of computation time for crack cutting.

#cutting tests	#cutting events	computation time (sec)		time ratio
		proposed	Delaunay	
1000	837	0.0165554	0.0384098	2.32
5000	4260	0.057322	0.1843772	3.22
10000	8470	0.120299	0.3865777	3.21
100000	84699	1.1720987	3.7420633	3.19
1000000	847407	14.08104	46.020675	3.27

The computation time for the proposed templated cutting method and the Delaunay triangulation method is collected in Table 8. From the table we can easily observe that the proposed templated cutting method is much faster than the Delaunay triangulation method. The time ratio of the two methods is about 3. The efficiency of the proposed templated cutting method is highly demonstrated. It is also worth mentioning that the proposed templated cutting method is quite robust since no cumbersome geometric implementations are introduced.

7.2.3. Efficiency in terms of overall computations

We use the example of double edge cracks, as presented in Section 7.1.1, to examine the overall computational efficiency of IXFEM. The tested cases are selected from the enrichment convergence studies, which include the cases with enrichment radii (R_e) ranging from $1h$ to $5h$. As for $R_e \geq 5h$, no convergence is observed for both XFEM and CXFEM with an iterative linear system solver (BiCG) when a maximum number of iterations (500,000) is reached. The convergence tolerance is intentionally set to a large value of 10^{-6}. In the tests, the level set templated cover cutting method is used for description of cracks in all the three XFEMs.

The test results in terms of computational time distribution are presented in Table 9 for $R_e \leq 5h$. This table shows (1) the time cost for stiffness matrix generation (including the time to calculate element stiffness matrices and the time to assemble global stiffness matrix), (2) the time cost for linear system solving (LSS), and (3) the time cost for remaining operations (including the time to discretize the crack, the time to apply boundary conditions, etc.). The total time cost for overall computations is also presented. From this table, we can conclude that:

(1) IXFEM costs (one order of magnitude) more time than XFEM and CXFEM in stiffness matrix generation. Since the extra-dof-free singularity enrichment needs to calculate the inverses of small-scale dense matrices (seven-order in 2D), IXFEM theoretically consumes more expenses than XFEM and CXFEM in terms of element stiffness calculations.
(2) IXFEM costs far less time than XFEM and CXFEM in linear system solving (LSS) with an iterative solver (*de facto* in large-scale simulations). Especially for geometrical enrichment, the time cost for LSS with XFEM and CXFEM grows unbounded due to slow convergence or failure of convergence.

Table 9
Computational time distribution for the three XFEMs with different enrichment radii (R_e).

Method	Time (s)	$R_e = 1h$	$2h$	$3h$	$4h$	$5h$
XFEM	t_{KEG}[a]	0.236	0.252	0.286	0.324	0.393
	t_{LSS}[b]	0.085	0.538	2.750	62.757	N.A.[e]
	t_{RMN}[c]	0.119	0.123	0.122	0.125	N.A.[e]
	t_{TOT}[d]	0.440	0.913	3.158	63.206	N.A.[e]
CXFEM	t_{KEG}[a]	0.262	0.295	0.338	0.396	0.483
	t_{LSS}[b]	1.744	10.936	45.281	N.A.[e]	N.A.[e]
	t_{RMN}[c]	0.119	0.122	0.122	N.A.[e]	N.A.[e]
	t_{TOT}[d]	2.125	11.353	45.741	N.A.[e]	N.A.[e]
IXFEM	t_{KEG}[a]	1.861	3.159	4.320	5.522	7.590
	t_{LSS}[b]	0.064	0.064	0.069	0.068	0.070
	t_{RMN}[c]	0.117	0.118	0.121	0.123	0.126
	t_{TOT}[d]	2.042	3.341	4.510	5.713	7.786

[a] t_{KEG} = time cost for (elemental and global) stiffness matrix generation.
[b] t_{LSS} = time cost for linear system solving (LSS).
[c] t_{RMN} = time cost for remaining operations.
[d] t_{TOT} = total time cost for overall computations.
[e] N.A. = not available due to failure of convergence in LSS.

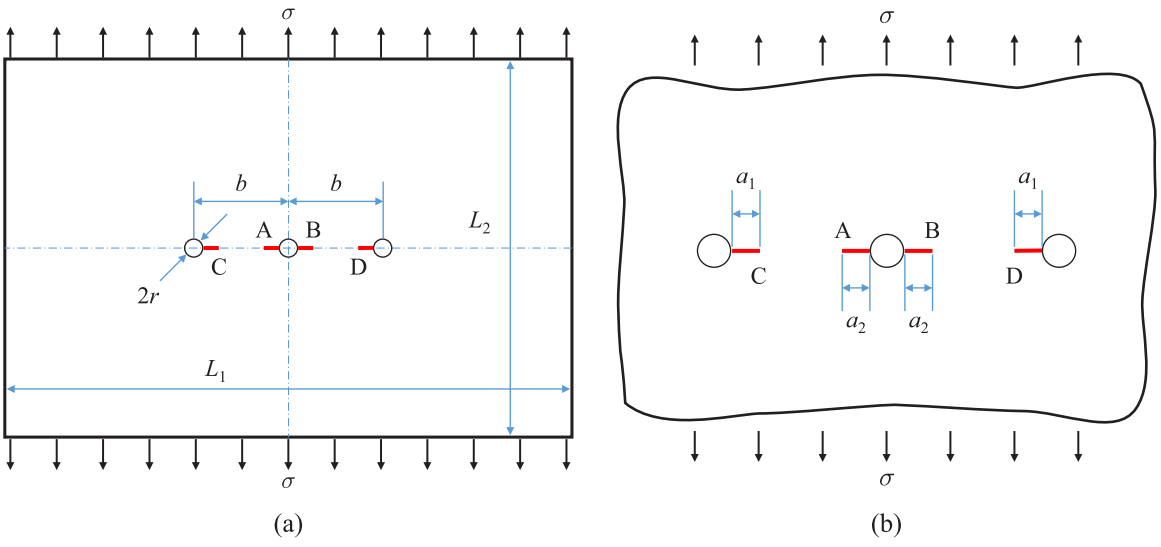

Fig. 28. Analyzed configuration with multiple cracks: (a) model setup; (b) crack lengths.

(3) The total time cost for the three XFEMs differs with the enrichment radius (R_e). When R_e is small, XFEM costs less time than IXFEM, but when R_e is large, XFEM costs much more time than IXFEM. Among the three XFEMs, CXFEM cost the most time whether R_e is large or small.

7.3. Engineering example

A typical aero structural configuration in engineering practices demonstrates the last example, which was presented by Kastratović et al. [90] to validate their approximate procedure to evaluate SIFs. The configuration is used to simulate multiple site damage (MSD) of great interest in aero community, which can be very serious because of possible linkup of adjacent cracks and can cause catastrophic failure once a large crack is formed.

The configuration, as shown in Fig. 28, is a thin plate with three circular holes subjected to uniform uniaxial tensile stress σ. The middle hole has two radial cracks while the other two have one radial crack. The material of

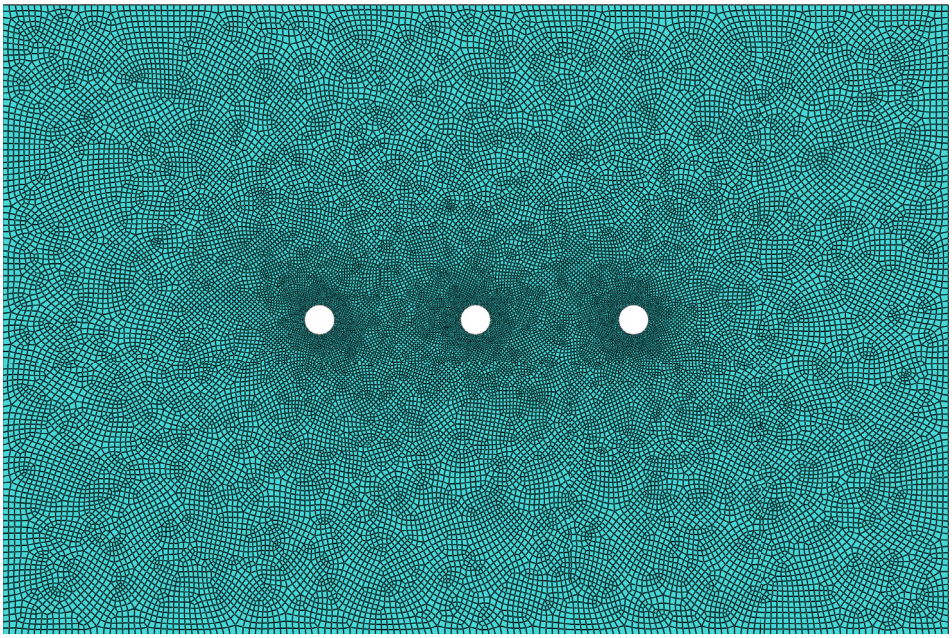

Fig. 29. Simulation mesh for IXFEM.

the plate is aluminum alloy Al-2024 T3. Since small-strain yielding conditions prevail in the vicinity of crack tips, the material is considered isotropic linear elastic and the simulation is conducted under the LEFM framework.

The dimensions of the plate are $L_1 \times L_2$, the radius of the three holes is r, the distance between two adjacent holes is b, and the length of the four cracks is either a_1 (cracks A and B) or a_2 (cracks C and D). The SIFs at the four crack tips are normalized as follows

$$\beta_{\mathrm{A}} = \frac{K_{\mathrm{IA}}}{\sigma\sqrt{\pi a_1}}, \quad \beta_{\mathrm{B}} = \frac{K_{\mathrm{IB}}}{\sigma\sqrt{\pi a_1}}, \quad \beta_{\mathrm{C}} = \frac{K_{\mathrm{IC}}}{\sigma\sqrt{\pi a_2}}, \quad \beta_{\mathrm{D}} = \frac{K_{\mathrm{ID}}}{\sigma\sqrt{\pi a_2}} \tag{59}$$

In the computations, the dimensions of the plate are taken as $L_1 = 150$ mm and $L_2 = 100$ mm. The radius of the holes is taken as $r = 2.4$ mm. The distance between two adjacent holes is taken as $b = 25$ mm. The crack length a_1 ranges from 1.00 mm to 8.00 mm while a_2 ranges from 1.00 mm to 4.80 mm. The material parameters are taken as: Young's modulus $E = 73$ GPa and Poisson's ratio $\nu = 0.33$. The simulation mesh for IXFEM, as shown in Fig. 29, contains 33,344 nodes and 33,006 quadrilateral elements.

In the work of Kastratović et al. [90], they compared SIF results obtained by their approximate procedure against results obtained through calculation with two finite element software packages. One is the FEM software package ANSYS v14; the other is an Abaqus plug-in Morfeo/Crack based on the standard XFEM. SIFs in ANSYS were calculated by displacement extrapolation technique while SIFs in Morfeo were extracted through interaction integrals. The three sets of available SIF solutions, namely the approximate solutions, the ANSYS solutions and the Morfeo solutions, are taken herein for comparison purposes.

The SIFs are calculated for a series of models with different crack lengths for all the cracks in the configuration. The crack increment is set to be the same for all the cracks based on the service data which shows that cracks in MSD are roughly of equal length. The normalized SIFs (denoted as β) for all the cracks are tabulated in Tables 10 and 11. The curves of normalized SIF versus dimensionless crack length are plotted in Fig. 30.

As can be seen from the figure, excellent agreements between SIF results by IXFEM and by other methods are achieved. In particular, the SIFs for crack tips A and B obtained by IXFEM nearly coincide with those obtained by ANSYS. The average difference between IXFEM and ANSYS with regard to crack A is merely 0.9% and the average difference between IXFEM and ANSYS with regard to crack B is merely 1.2%. The average differences between IXFEM and Morfeo are 2.1% for crack A and 3.2% for crack B, respectively. The average differences between IXFEM and the approximate procedure are 3.0% for crack A and 2.6% for crack B, respectively.

Table 10
Comparison of the SIF solutions for crack tips A and B.

a_1 (mm)	r (mm)	b (mm)	a_2 (mm)	β_A-IXFEM	β_B-IXFEM	β-Approx.[a]	β-ANSYS[a]	β_A-Morfeo[a]	β_B-Morfeo[a]
1.00	2.4	25	1.00	1.9197	1.9102	1.9490	1.9736	1.7691	1.8046
1.60	2.4	25	1.53	1.6765	1.6741	1.6584	1.6969	1.6787	1.6658
2.00	2.4	25	1.86	1.5959	1.5691	1.5424	1.5951	1.5823	1.6267
2.60	2.4	25	2.28	1.4828	1.4462	1.4289	1.4849	1.5072	1.5206
3.00	2.4	25	2.53	1.4335	1.4284	1.3778	1.4285	1.4378	1.4614
3.60	2.4	25	2.87	1.3595	1.3577	1.3234	1.3701	1.3954	1.4152
4.00	2.4	25	3.00	1.3287	1.3273	1.2960	1.3467	1.3522	1.3729
5.00	2.4	25	3.56	1.2994	1.2943	1.2546	1.2974	1.3221	1.3510
6.00	2.4	25	4.00	1.2675	1.2702	1.2323	1.2728	1.3062	1.3065
7.00	2.4	25	4.43	1.2661	1.2658	1.2242	1.2548	1.2766	1.3092
8.00	2.4	25	4.80	1.2772	1.2755	1.2262	1.2545	1.2546	1.2640

[a]These SIF solutions are taken from Kastratović et al. [90].

Table 11
Comparison of the SIF solutions for crack tips C and D.

a_1 (mm)	r (mm)	b (mm)	a_2 (mm)	β_C-IXFEM	β_D-IXFEM	β-Approx.[a]	β-ANSYS[a]	β_C-Morfeo[a]	β_D-Morfeo[a]
1.00	2.4	25	1.00	1.8246	1.7985	1.8615	1.9736	1.8091	1.7786
1.60	2.4	25	1.53	1.5636	1.5570	1.6061	1.6969	1.6146	1.6351
2.00	2.4	25	1.86	1.4735	1.4675	1.5002	1.5951	1.5470	1.5384
2.60	2.4	25	2.28	1.3738	1.3687	1.4006	1.4849	1.4195	1.4361
3.00	2.4	25	2.53	1.3475	1.3297	1.3551	1.4285	1.3676	1.3820
3.60	2.4	25	2.87	1.2996	1.2884	1.3060	1.3701	1.3414	1.3288
4.00	2.4	25	3.00	1.2926	1.2773	1.2930	1.3467	1.3402	1.3274
5.00	2.4	25	3.56	1.2551	1.2293	1.2442	1.2974	1.2900	1.2571
6.00	2.4	25	4.00	1.2202	1.2224	1.2288	1.2728	1.2357	1.2418
7.00	2.4	25	4.43	1.2317	1.2344	1.2318	1.2548	1.2521	1.2305
8.00	2.4	25	4.80	1.2685	1.2582	1.2573	1.2545	1.2431	1.2471

[a]These SIF solutions are taken from Kastratović et al. [90].

For cracks C and D, there are also good agreements between SIF results by IXFEM and by other methods. From the figure we can see that IXFEM is very close to the approximate procedure. The average difference between IXFEM and the approximate procedure with regard to crack C is merely 1.1% and the average difference between IXFEM and the approximate procedure with regard to crack D is merely 1.6%. The average differences between IXFEM and ANSYS are 5.1% for crack C and 5.6% for crack D, respectively. The average differences between IXFEM and Morfeo are 1.1% for crack C and 5.6% for crack D, respectively. Considering that different meshes and methods are used, an average difference of order 5% is quite reasonable.

From the above observations we can conclude that the SIF solutions obtained by IXFEM are absolutely acceptable from an engineering point of view. Thus the approach proposed in this paper provides a very capable tool for multiple crack analysis.

8. Conclusions

Stress intensity factor (SIF) plays a critical role in LEFM analysis because it is the single parameter that represents the singular field at the crack tip. Thus, accurate calculation of SIFs, in particular for multiple cracks, is quite essential for the prediction of crack growth rate and residual strength of cracked structures.

To meet this end, we develop an improved XFEM (IXFEM) with novel geometric description for multiple cracks. The proposed approach, on the one hand, avoids the difficulty of level set combination in XFEM by introducing templated cover cutting; and on the other hand, eliminates the daunting issues of linear dependence and ill-conditioning of XFEM by employing an extra-dof-free singularity enrichment around a crack tip. The developed approach shows promising insight into multiple crack analysis.

Several benchmark problems are considered in terms of SIF accuracy, linear system solving efficiency, geometric computation efficiency and overall computation efficiency. An engineering example of a typical aero structural

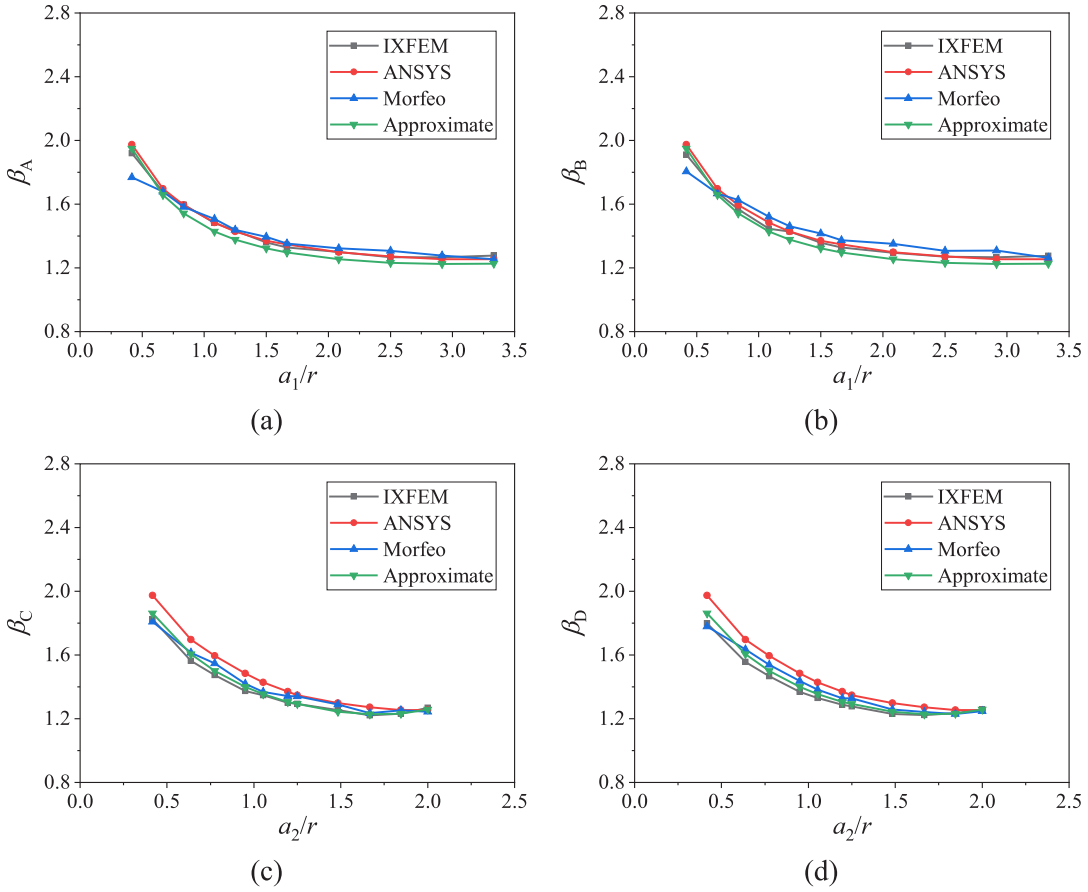

Fig. 30. Normalized SIFs for (a) crack tip A, (b) crack tip B, (c) crack tip C and (d) crack tip D. Reference SIF solutions are taken from [90].

configuration is also demonstrated. Comparative studies with available SIF solutions or existing numerical methods are carried out. New findings with regard to multiple crack problems are revealed on IXFEM. Conclusions are drawn as follows:

(1) IXFEM offers highly accurate SIF evaluation over the standard and corrected XFEMs in a multiple crack simulation. From the SIF benchmarks we can see that the SIF errors of IXFEM are significantly lower than those of XFEM and slightly lower than those of CXFEM. IXFEM always generates SIF results closer to theoretical solutions.

(2) IXFEM exhibits well-conditioning of the global stiffness matrix independent of the number of cracks. When this number increases, the ill-conditioning of XFEM and in particular CXFEM becomes even more severe. Since IXFEM utilizes an extra-dof-free singularity enrichment, it does not suffer from this daunting issue at all and recovers the well-conditioning as the standard FEM.

(3) In a multiple crack simulation, the three XFEMs all require iterations of order $O(\log(n_c))$ and time of order $O(\log^3(n_c))$ to solve systems of linear equations. The slope or major coefficient of IXFEM is much smaller than that of XFEM and CXFEM. This indicates that IXFEM consumes relatively less expense in linear system solving.

(4) The proposed level set templated cover cutting method is much more efficient than the Delaunay triangulation method. It is also quite robust since no cumbersome geometric implementations are introduced.

(5) IXFEM consumes one order of magnitude more time than XFEM and CXFEM in stiffness matrix generation. However, it costs far less time in linear system solving when an iterative solver is used. The total time spent

for overall computations depends on the enrichment radius. When the geometrical enrichment strategy is used, IXFEM shows its significant efficiency while maintaining high accuracy.

(6) From the last example we can see that the SIF solutions obtained by IXFEM are comparable with available software solutions from an engineering point of view. Thus, the proposed approach provides a very capable tool for multiple crack analysis.

On-going work is to investigate the proposed approach for multiple evolving crack problems, which involve initiation, propagation and interaction of arbitrary multiple cracks [91]. As no extra dofs and no cumbersome geometric implementations are required, the proposed approach should also be accurate, efficient, stable and robust for such problems. The extension of this approach to three-dimensional crack problems seems to be feasible as well and remains to be further investigated.

CRediT authorship contribution statement

Long-Fei Wen: Conceptualization, Methodology, Software, Validation, Writing – review & editing, Formal analysis, Data curation. **Rong Tian:** Methodology, Writing – review & editing, Formal analysis, Funding acquisition, Project administration. **Li-Xiang Wang:** Conceptualization, Methodology, Software, Validation, Writing – original draft, Writing – review & editing, Funding acquisition, Formal analysis, Data curation, Visualization. **Chun Feng:** Resources, Supervision, Writing – review & editing, Funding acquisition.

Declaration of competing interest

The authors declare that they have no known competing financial interests or personal relationships that could have appeared to influence the work reported in this paper.

Data availability

Data will be made available on request.

Acknowledgments

The authors gratefully acknowledge the financial support from the National Natural Science Foundation of China (Grant No. 12102059), the Science Challenge Project, China (Grant No. TZ2018002), and the National Key Research and Development Program of China (Grant No. 2018YFC1505504).

References

[1] L.X. Wang, D.H. Tang, S.H. Li, J. Wang, C. Feng, Numerical simulation of hydraulic fracturing by a mixed method in two dimensions, Chin. J. Theor. Appl. Mech. 47 (6) (2015) 973–983, http://dx.doi.org/10.6052/0459-1879-15-097.

[2] X.G. Zhu, C. Feng, P.D. Cheng, X.Q. Wang, S.H. Li, A novel three-dimensional hydraulic fracturing model based on continuum–discontinuum element method, Comput. Methods Appl. Mech. Engrg. 383 (2021) 113887.

[3] Y.T. Yang, X.H. Tang, H. Zheng, Q.S. Liu, Z.J. Liu, Hydraulic fracturing modeling using the enriched numerical manifold method, Appl. Math. Model. 53 (2018) 462–486.

[4] L.X. Wang, S.H. Li, G.X. Zhang, Z.S. Ma, L. Zhang, A GPU-based parallel procedure for nonlinear analysis of complex structures using a coupled FEM/DEM approach, Math. Probl. Eng. 2013 (2013) 618980, http://dx.doi.org/10.1155/2013/618980.

[5] R. Tian, M.Z. Zhou, J.T. Wang, Y. Li, H.B. An, X.W. Xu, L.F. Wen, L.X. Wang, Q. Xu, J.L. Leng, R. Xu, B.Y. Zhang, W.J. Liu, Z.Y. Mo, A challenging dam structural analysis: large-scale implicit thermo-mechanical coupled contact simulation on Tianhe-II, Comput. Mech. 63 (2019) 99–119.

[6] X.L. Li, Z.M. Hao, On deformation and fracture of PBX simulant employing modified three-body potential peridynamics model with deformation-based failure criteria, Appl. Math. Model. 115 (2023) 100–126.

[7] K. Yakoubi, S. Montassir, H. Moustabchir, A. Elkhalfi, C.I. Pruncu, J. Arbaoui, M.U. Farooq, An extended finite element method (XFEM) study on the elastic T-stress evaluations for a notch in a pipe steel exposed to internal pressure, Mathematics 9 (2021) 507.

[8] H. Tada, P.C. Paris, G.R. Irwin, The Stress Analysis of Cracks Handbook, Del Research Corporation, Hellertown, Pennsylvania, USA, 1973.

[9] H. Tada, P.C. Paris, G.R. Irwin, The Stress Analysis of Cracks Handbook second ed., Paris Productions Inc., St. Louis, USA, 1985.

[10] H. Tada, P.C. Paris, G.R. Irwin, The Stress Analysis of Cracks Handbook, third ed., ASME Press, New York, USA, 2000.

[11] Y. Murakami (Ed.), Stress Intensity Factors Handbook, Vols. 1, 2, Pergamon Press, Oxford etc, 1987.

[12] Y. Murakami (Ed.), Stress Intensity Factors Handbook, Vol. 3, The Society of Materials Science, Japan, and Pergamon Press, 1992.

[13] Y. Murakami (Ed.), Stress Intensity Factors Handbook, Vols. 4, 5 The Society of Materials Science, Japan & Elsevier Science Ltd., 2001.
[14] E. Sari, M. Zergoug, FEM techniques comparison for SIF computing of cracked plate, Arab. J. Sci. Eng. 40 (2015) 1165–1171.
[15] X.Q. Yan, A boundary element analysis for stress intensity factors of multiple circular arc cracks in a plane elasticity plate, Appl. Math. Model. 34 (10) (2010) 2722–2737.
[16] Y.T. Yang, G.H. Sun, H. Zheng, A high-order numerical manifold method with continuous stress/strain field, Appl. Math. Model. 78 (2020) 576–600.
[17] J.T. Oden, C.A. Duarte, Clouds cracks and FEM's, in: B.D. Reddy (Ed.), Recent Developments in Computational and Applied Mechanics, International Center for Numerical Methods in Engineering, CIMNE, Barcelona, Spain, 1997, pp. 302–321.
[18] T. Strouboulis, I. Babuška, K. Copps, The design and analysis of the generalized finite element method, Comput. Methods Appl. Mech. Engrg. 181 (1–3) (2000) 43–69.
[19] C.A. Duarte, I. Babuška, J.T. Oden, Generalized finite element methods for three dimensional structural mechanics problems, Comput. Struct. 77 (2000) 215–232.
[20] M. Schätzer, T.P. Fries, Loaded crack surfaces in two and three dimensions with XFEM, Appl. Math. Model. 78 (2020) 863–885.
[21] M. Pant, I.V. Singh, B.K. Mishra, Evaluation of mixed mode stress intensity factors for interface cracks using EFGM, Appl. Math. Model. 35 (7) (2011) 3443–3459.
[22] S.S. Chen, W. Wang, X.S. Zhao, An interpolating element-free Galerkin scaled boundary method applied to structural dynamic analysis, Appl. Math. Model. 75 (2019) 494–505.
[23] M.S. Chowdhury, C.M. Song, W. Gao, Shape sensitivity analysis of stress intensity factors by the scaled boundary finite element method, Eng. Fract. Mech. 116 (2014) 13–30.
[24] C. Feng, X.M. Liu, Q.D. Lin, S.H. Li, A simple particle–spring method for capturing the continuous–discontinuous processes of brittle materials, Eng. Anal. Bound. Elem. 139 (2022) 221–231.
[25] K. Jiang, X.F. Zhu, C.Z. Hu, W.B. Hou, P. Hu, S.P.A. Bordas, An enhanced extended isogeometric analysis with strong imposition of essential boundary conditions for crack problems using B++ Splines, Appl. Math. Model. 116 (2023) 393–414.
[26] V.M. Nguyen-Thanh, X.Y. Zhuang, H. Nguyen-Xuan, T. Rabczuk, P. Wriggers, A Virtual Element Method for 2D linear elastic fracture analysis, Comput. Methods Appl. Mech. Engrg. 340 (2018) 366–395.
[27] Y.M. Zhang, X.Y. Zhuang, Cracking elements: A self-propagating strong discontinuity embedded approach for quasi-brittle fracture, Finite Elem. Anal. Des. 144 (2018) 84–100.
[28] T. Belytschko, T. Black, Elastic crack growth in finite elements with minimal remeshing, Internat. J. Numer. Methods Engrg. 45 (5) (1999) 601–620.
[29] N. Moës, J. Dolbow, T. Belytschko, A finite element method for crack growth without remeshing, Internat. J. Numer. Methods Engrg. 46 (1) (1999) 131–150.
[30] Abaqus 6.9 Documentation, Analysis User's Manual, Section 10.6.1, Dassault Systèmes Simulia Corp, 2009.
[31] ANSYS Mechanical APDL Fracture Analysis Guide, ANSYS Inc. 2015.
[32] T. Belytschko, R. Gracie, G. Ventura, A review of extended/generalized finite element methods for material modeling, Modelling Simul. Mater. Sci. Eng. 17 (2009) 043001.
[33] T.P. Fries, T. Belytschko, The extended/generalized finite element method: an overview of the method and its applications, Internat. J. Numer. Methods Engrg. 84 (3) (2010) 253–304.
[34] I. Babuška, U. Banerjee, Stable generalized finite element method (SGFEM), Comput. Methods Appl. Mech. Engrg. 201–204 (2012) 91–111.
[35] A. Sillem, A. Simone, L. Sluys, The Orthonormalized Generalized Finite Element Method–OGFEM: Efficient and stable reduction of approximation errors through multiple orthonormalized enriched basis functions, Comput. Methods Appl. Mech. Engrg. 287 (2015) 112–149.
[36] K. Agathos, E. Chatzi, S.P.A. Bordas, D. Talaslidis, A well-conditioned and optimally convergent XFEM for 3D linear elastic fracture, Internat. J. Numer. Methods Engrg. 105 (9) (2015) 643–677.
[37] K. Agathos, S.P.A. Bordas, E. Chatzi, Improving the conditioning of XFEM/GFEM for fracture mechanics problems through enrichment quasi-orthogonalization, Comput. Methods Appl. Mech. Engrg. 346 (2019) 1051–1073.
[38] V. Gupta, C.A. Duarte, I. Babuška, U. Banerjee, A stable and optimally convergent generalized FEM (SGFEM) for linear elastic fracture mechanics, Comput. Methods Appl. Mech. Engrg. 266 (2013) 23–39.
[39] V. Gupta, C.A. Duarte, I. Babuška, U. Banerjee, Stable GFEM (SGFEM): Improved conditioning and accuracy of GFEM/XFEM for three-dimensional fracture mechanics, Comput. Methods Appl. Mech. Engrg. 289 (2015) 355–386.
[40] J. Réthoré, A. Gravouil, A. Combescure, An energy-conserving scheme for dynamic crack growth using the extended finite element method, Internat. J. Numer. Methods Engrg. 63 (2005) 631–659.
[41] B. Prabel, A. Combescure, A. Gravouil, S. Marie, Level set X-FEM non-matching meshes: Application to dynamic crack propagation in elastic–plastic media, Internat. J. Numer. Methods Engrg. 69 (2007) 1553–1569.
[42] A. Combescure, A. Gravouil, D. Grégoire, J. Réthoré, X-FEM a good candidate for energy conservation in simulation of brittle dynamic crack propagation, Comput. Methods Appl. Mech. Engrg. 197 (2008) 309–318.
[43] H. Zheng, Y.T. Yang, G.H. Shi, Reformulation of dynamic crack propagation using the numerical manifold method, Eng. Anal. Bound. Elem. 105 (2019) 279–295.
[44] R. Tian, L.F. Wen, Improved XFEM—An extra-dof free, well-conditioning, and interpolating XFEM, Comput. Methods Appl. Mech. Engrg. 285 (2015) 639–658.
[45] L.F. Wen, R. Tian, Improved XFEM: Accurate and robust dynamic crack growth simulation, Comput. Methods Appl. Mech. Engrg. 308 (2016) 256–285.

[46] L.X. Wang, L.F. Wen, J.T. Wang, R. Tian, Implementations of parallel software for crack analyses based on the improved XFEM, Sci. Sin. Tech. 48 (11) (2018) 1241–1258, http://dx.doi.org/10.1360/N092017-00367.
[47] R. Tian, L.F. Wen, L.X. Wang, Three-dimensional improved XFEM (IXFEM) for static crack problems, Comput. Methods Appl. Mech. Engrg. 343 (2019) 339–367.
[48] G.Z. Xiao, L.F. Wen, R. Tian, Arbitrary 3D crack propagation with Improved XFEM: Accurate and efficient crack geometries, Comput. Methods Appl. Mech. Engrg. 377 (2021) 113659.
[49] G.Z. Xiao, L.F. Wen, R. Tian, D.G. Zhang, Improved XFEM (IXFEM): 3D dynamic crack propagation under impact loading, Comput. Methods Appl. Mech. Engrg. 405 (2023) 115844.
[50] R. Tian, Extra-dof-free and linearly independent enrichments in GFEM, Comput. Methods Appl. Mech. Engrg. 266 (2013) 1–22.
[51] C. Daux, N. Moës, J. Dolbow, N. Sukumar, T. Belytschko, Arbitrary branched and intersecting cracks with the extended finite element method, Internat. J. Numer. Methods Engrg. 48 (12) (2000) 1741–1760.
[52] T. Belytschko, N. Moës, S. Usui, C. Parimi, Arbitrary discontinuities in finite elements, Internat. J. Numer. Methods Engrg. 50 (4) (2001) 993–1013.
[53] É. Budyn, G. Zi, N. Moës, T. Belytschko, A method for multiple crack growth in brittle materials without remeshing, Internat. J. Numer. Methods Engrg. 61 (10) (2004) 1741–1770.
[54] G. Zi, J.H. Song, E. Budyn, S.H. Lee, T. Belytschko, A method for growing multiple cracks without remeshing and its application to fatigue crack growth, Modelling Simul. Mater. Sci. Eng. 12 (2004) 901–915.
[55] S.E. Mousavi, E. Grinspun, N. Sukumar, Harmonic enrichment functions: A unified treatment of multiple, intersecting and branched cracks in the extended finite element method, Internat. J. Numer. Methods Engrg. 85 (10) (2011) 1306–1322.
[56] C.L. Richardson, J. Hegemann, E. Sifakis, J. Hellrung, J.M. Teran, An XFEM method for modeling geometrically elaborate crack propagation in brittle materials, Internat. J. Numer. Methods Engrg. 88 (10) (2011) 1042–1065.
[57] D.D. Xu, Z.L. Liu, X.M. Liu, Q.L. Zeng, Z. Zhuang, Modeling of dynamic crack branching by enhanced extended finite element method, Comput. Mech. 54 (2014) 489–502.
[58] D. Sutula, P. Kerfriden, T. van Dam, S.P.A. Bordas, Minimum energy multiple crack propagation. Part I: Theory and state of the art review, Eng. Fract. Mech. 191 (2018) 205–224.
[59] D. Sutula, P. Kerfriden, T. van Dam, S.P.A. Bordas, Minimum energy multiple crack propagation. Part-II: Discrete solution with XFEM, Eng. Fract. Mech. 191 (2018) 225–256.
[60] D. Sutula, P. Kerfriden, T. van Dam, S.P.A. Bordas, Minimum energy multiple crack propagation. Part III: XFEM computer implementation and applications, Eng. Fract. Mech. 191 (2018) 257–276.
[61] J.W. Chen, X.P. Zhou, The enhanced extended finite element method for the propagation of complex branched cracks, Eng. Anal. Bound. Elem. 104 (2019) 46–62.
[62] J.H. Song, P.M.A. Areias, T. Belytschko, A method for dynamic crack and shear band propagation with phantom nodes, Internat. J. Numer. Methods Engrg. 67 (6) (2006) 868–893.
[63] J.L. Ding, T.T. Yu, T.Q. Bui, Modeling strong/weak discontinuities by local mesh refinement variable-node XFEM with object-oriented implementation, Theor. Appl. Fract. Mech. 106 (2020) 102434.
[64] J.L. Ding, T.T. Yu, Y. Yang, T.Q. Bui, An efficient variable-node XFEM for modeling multiple crack growth: A matlab object-oriented implementation, Adv. Eng. Softw. 140 (2020) 102750.
[65] A. Jafari, P. Broumand, M. Vahab, N. Khalili, An eXtended finite element method implementation in COMSOL multiphysics: Solid mechanics, Finite Elem. Anal. Des. 202 (2022) 103707.
[66] G.H. Shi, Manifold method of material analysis, in: Transactions of the 9th Army Conference on Applied Mathematics and Computing, Minneapolis, Minnesota, 1991, pp. 57–76.
[67] G.W. Ma, X.M. An, H.H. Zhang, L.X. Li, Modeling complex crack problems using the numerical manifold method, Int. J. Fract. 156 (2009) 21–35.
[68] G.W. Ma, X.M. An, L. He, The numerical manifold method: A review, Int. J. Comput. Methods 7 (1) (2010) 1–32.
[69] H. Zheng, F. Liu, X.L. Du, Complementarity problem arising from static growth of multiple cracks and MLS-based numerical manifold method, Comput. Methods Appl. Mech. Engrg. 295 (2015) 150–171.
[70] S. Kumar, I.V. Singh, B.K. Mishra, T. Rabczuk, Modeling and simulation of kinked cracks by virtual node XFEM, Comput. Methods Appl. Mech. Engrg. 283 (2015) 1425–1466.
[71] J. Dolbow, N. Moës, T. Belytschko, Discontinuous enrichment in finite elements with a partition of unity method, Finite Elem. Anal. Des. 36 (2000) 235–260.
[72] A.G. Sanchez-Rivadeneira, C.A. Duarte, A stable generalized/eXtended FEM with discontinuous interpolants for fracture mechanics, Comput. Methods Appl. Mech. Engrg. 345 (2019) 876–918.
[73] T.P. Fries, A corrected XFEM approximation without problems in blending elements, Internat. J. Numer. Methods Engrg. 75 (5) (2008) 503–532.
[74] T. Belytschko, D. Organ, Y. Krongauz, A coupled finite element–element-free Galerkin method, Comput. Mech. 17 (1995) 186–195.
[75] L.X. Wang, L.F. Wen, G.Z. Xiao, R. Tian, A templated method for partitioning of solid elements in discontinuous problems, Chin. J. Theor. Appl. Mech. 53 (3) (2021) 823–836, http://dx.doi.org/10.6052/0459-1879-20-360.
[76] T.P. Fries, T. Belytschko, The extended/generalized finite element method: An overview of the method and its applications, Internat. J. Numer. Methods Engrg. 84 (3) (2010) 253–304.
[77] S.E. Mousavi, N. Sukumar, Generalized Gaussian quadrature rules for discontinuities and crack singularities in the extended finite element method, Comput. Methods Appl. Mech. Engrg. 199 (2010) 3237–3249.
[78] A.R. Khoei, Extended Finite Element Method: Theory and Applications, John Wiley & Sons, Ltd. 2015.

[79] B.C. Campos, F.B. Barros, S.S. Penna, On the numerical integration in generalized/extended finite element method analysis for crack propagation problems, Eng. Comput. 38 (1) (2021) 180–220.
[80] C.F. Shih, H.G. de Lorenzi, M.D. German, Crack extension modeling with singular quadratic isoparametric elements, Int. J. Fract. 12 (1976) 647–651.
[81] D.M. Parks, A stiffness derivative finite element technique for determination of crack tip stress intensity factors, Int. J. Fract. 10 (1974) 487–502.
[82] E.F. Rybicki, M. Kanninen, A finite element calculation of stress intensity factors by a modified crack closure integral, Eng. Fract. Mech. 9 (4) (1977) 931–938.
[83] Z. Kang, T.Q. Bui, D.D. Nguyen, T. Saitoh, S. Hirose, An extended consecutive-interpolation quadrilateral element (XCQ4) applied to linear elastic fracture mechanics, Acta Mech. 226 (2015) 3991–4015.
[84] J.R. Rice, A path independent and the approximate analysis of strain concentration by notches and cracks, J. Appl. Mech. 35 (2) (1968) 379–386.
[85] T.L. Anderson, Fracture Mechanics: Fundamentals and Applications, CRC Press, 2017.
[86] Y. Chen, N. Hasebe, New integration scheme for the branch crack problem, Eng. Fract. Mech. 52 (5) (1995) 791–801.
[87] Y.K. Cheung, C.W. Woo, Y.H. Wang, A general method for multiple crack problems in a finite plate, Comput. Mech. 10 (5) (1992) 335–343.
[88] J.C. Newman Jr., An Improved Method of Collocation for the Stress Analysis of Cracked Plates with Various Shaped Boundaries, NASA Technical Note, Report No. NASA TN D-6376, 1971.
[89] S. Balay, S. Abhyankar, M.F. Adams, S. Benson, J. Brown, P. Brune, K. Buschelman, E.M. Constantinescu, L. Dalcin, A. Dener, V. Eijkhout, J. Faibussowitsch, W.D. Gropp, V. Hapla, T. Isaac, P. Jolivet, D. Karpeev, D. Kaushik, M.G. Knepley, F. Kong, S. Kruger, D.A. May, L.C. McInnes, R.T. Mills, L. Mitchell, T. Munson, J.E. Roman, K. Rupp, P. Sanan, J. Sarich, B.F. Smith, S. Zampini, H. Zhang, H. Zhang, J. Zhang, PETSc/TAO Users Manual, Argonne National Laboratory, 2022, ANL-21/39 - Revision 3.18.
[90] G. Kastratović, A. Grbović, N. Vidanović, Approximate method for stress intensity factors determination in case of multiple site damage, Appl. Math. Model. 39 (19) (2015) 6050–6059.
[91] L.X. Wang, R. Tian, L.F. Wen, C. Feng, Improved XFEM (IXFEM): Arbitrary multiple crack initiation, propagation and interaction analysis (in preparation).